Astronomy & Astrophysics

Long slit spectroscopy of a sample of isolated spirals with and without an AGN[*],[**],[***]

I. Márquez[1], F. Durret[2], J. Masegosa[1], M. Moles[1], J. Varela[1], R. M. González Delgado[1], J. Maza[3], E. Pérez[1], and M. Roth[4]

[1] Instituto de Astrofísica de Andalucía (CSIC), Apartado 3004 , 18080 Granada, Spain
[2] Institut d'Astrophysique de Paris, CNRS, 98bis Bd Arago, 75014 Paris, France
[3] Departamento de Astronomía, Universidad de Chile, Casilla 36D, Santiago, Chile
[4] Observatories of the Carnegie Institution of Washington, 813 Barbara Street, Pasadena, CA91101, USA

Abstract. We present the kinematical data obtained for a sample of active (Seyfert) and non active isolated spiral galaxies, based on long slit spectra along several position angles in the Hα line region and, in some cases, in the Ca triplet region as well. Gas velocity distributions are presented, together with a simple circular rotation model that allows us to determine the kinematical major axes. Stellar velocity distributions are also shown. The main result is that active and control galaxies seem to be equivalent in all kinematical aspects. For both subsamples, the departure from pure circular rotation in some galaxies can be explained by the presence of a bar and/or of a spiral arm. They also present the same kind of peculiarities, in particular, S-shape structures are quite common near the nuclear regions. They define very similar Tully-Fisher relations. Emission line ratios are given for all the detected HII regions; the analysis of the [NII]/Hα metallicity indicator shows that active and non-active galaxies have indistinguishable disk metallicities. These results argue in favour of active and non-active isolated spiral galaxies having essentially the same properties, in agreement with our previous results based on the analysis of near infrared images. It appears now necessary to confirm these results on a larger sample.

Key words. galaxies: spiral – galaxies: kinematics and dynamics – galaxies: structure – galaxies: interactions

1. Introduction

The DEGAS collaboration was started a few years ago to search for a sufficient condition for a galaxy to host an active nucleus. The active galaxies have been chosen with the following criteria: (a) catalogued as Seyfert 1 or 2 in Véron-Cetty & Véron's catalogue (we have checked that they were all classified as Seyferts in the NED database and give their AGN type in Table 1); (b) with morphological information in the RC3 catalogue (de Vaucouleurs et al. 1991); (c) isolated, in the sense of not having a companion within 0.4 Mpc

($H_0 = 75$ km s^{-1} Mpc^{-1}) and $cz < 500$ km s^{-1}, or companions catalogued by Nilson without known redshift; (d) nearby, $cz < 6000$ km s^{-1}; and (e) intermediate inclination (30 to 65°). Note however that the sample of active galaxies thus defined may not be representative of the whole AGN population, since the selection criteria of the Véron-Cetty & Véron catalogue are not necessarily complete. The non-active galaxies have been selected among spirals satisfying the same conditions (b), (c), (d) and (e), and with morphologies (given by the complete de Vaucouleurs coding, not just the Hubble type) similar to those of the active spirals. A total of 17 active galaxies and 16 non active galaxies (used as control sample), with similar distribution of morphological types (including the bar type), were selected. Since all galaxies were chosen to be isolated under the criteria defined above, side effects that could be produced by the gravitational interaction with nearby galaxies are avoided. The details of the program and sample definition are given in Márquez et al. (1999, 2000), where it has been shown that the non-active galaxies are well suited to be used as a control sample. Basic properties of the galaxies of our sample are given in Table 1. The observations we carried out included infrared and optical imaging and long slit spectroscopy to derive the kinematical properties of the ionized gas and, for

---

some of them, of the stellar component. Infrared HST images of our selected galaxies were also retrieved and analyzed when available.

The data already presented have shown some interesting results: the analysis of the infrared images indicated that there are no morphological differences between active and non active galaxies in our sample. We also found that most galaxies have bars and sometimes nuclear bars within the large bars. Some of these inner bars were reported for the first time (Márquez et al. 1999, 2000). The full analysis of NGC 6951, the first galaxy of our sample for which all the required data became available (Pérez et al. 2000), led us to discover the decoupling between the stellar and gas kinematics in the central regions, and to hint the presence of a younger stellar population there. Velocity drops were detected in the nuclear regions of five of our sample galaxies. The analysis of the calcium triplet (CaT) lines equivalent widths indicated the presence of a different stellar population spatially coincident with the kinematical drops. Further analysis of the HST images of a total of 14 galaxies with reported velocity dispersion drops (including our five), show evidence for central elongations in most of them, which could be related with the mechanism invoked in numerical models to reproduce such drops (see Márquez et al. 2003 and references therein).

The present work includes the kinematical data on the gas and stars obtained for the galaxies of our sample, together with the emission line ratios measured in the nuclear and extra-nuclear HII regions of the same galaxies. The metallicities of these HII regions, estimated from the observed line ratios, are briefly discussed. A general discussion based on the DEGAS data will be presented in a forthcoming paper.

The paper is organized as follows. The observations and data reduction procedures are presented in Sect. 2. Characteristics of the rotation curves for each galaxy, together with a discussion of the positions of our sample galaxies in the Tully-Fisher relation are presented in Sect. 3. The properties of nuclear and extra-nuclear HII regions are described in Sect. 4. The summary and conclusions are presented in Sect. 5.

2. Observations and data reduction

The spectroscopic data were collected with four different instruments: the Boller & Chivens spectrograph attached to the 1.5 m ESO telescope at La Silla (Chile), the Modular Spectrograph at the 2.5 m Dupont telescope at Las Campanas (Chile), the ISIS Spectrograph at the 4.2 m William Herschel telescope in La Palma (Spain) and the TWIN Spectrograph attached to the 3.5 m telescope in Calar Alto (CAHA, Spain). The setup and main characteristics of the observations are given in Table 2.

Standard IRAF[1] procedures were used for the reduction of the spectroscopic data, following the standard steps of bias

---

[1] IRAF is the Image Analysis and Reduction Facility made available to the astronomical community by the National Optical Astronomy Observatories, which are operated by the Association of Universities for Research in Astronomy (AURA), Inc., under contract with the US National Science Foundation.

Table 1. Main properties of the galaxies.

Galaxy	Type (RC3) (1)	m_B (mag) (2)	AGN type (3)
UGC 1395	.SAT3..	14.18	1.9
IC 184	.SBR1*.	14.66	2
IC 1816	.SBR2P?	13.83	1
UGC 3223	.SB.1..	13.83	1
NGC 2639	RSAR1*	12.59	1.9
IC 2510	.SBT2*.	14.00*	2
NGC 3660	.SBR4..	12.29	2
NGC 4507	PSXT3..	12.78	2
NGC 4785	PSBR3*.	13.21	2
NGC 5347	PSBT2..	13.16	2
NGC 5728	.SXR1*.	12.37	2
ESO139-12	PSAT4P*	13.59	2
NGC 6814	.SXT4..	11.85	1.5
NGC 6860	PSBR3..	13.68	1
NGC 6890	.SAT3..	13.05	2
NGC 6951	.SXT4..	11.91	2
NGC 151	.SBR4..	12.23	
NGC 1357	.SAS2..	12.46	
IC 454	.SB.2..	14.50*	
NGC 2712	.SBR3*.	12.38	
NGC 2811	.SBT1..	12.66	
NGC 3571	PSXT1*.	12.99	
NGC 3835	.S..2*/	13.20	
NGC 4162	RSAT4..	12.55	
NGC 4290	.SBT2*.	12.66	
NGC 6012	RSBR2*.	12.69	
NGC 6155	.S?....	13.20	
NGC 7328	.S..2..	13.98	

(1) Morphological type taken from the RC3 catalogue;
(2) B magnitude as given in the RC3 catalogue;
(3) AGN Seyfert type taken from the NED.
* Taken from NED.

subtraction, flat field correction, wavelength calibration with arc lamps observed before and after the target, atmospheric extinction correction, and flux calibration using spectroscopic standards observed through an 8 arcsec wide slit for WHT runs. The sky background level was determined taking median averages over two strips on either side of the galaxy signal. The parameters of the lines were measured with the program `splot`. The errors in Table 5 have been calculated by quadratic

Table 2. Observations.

Code	Telescope	Date	Instrument	Spectral sampling (Å/pix)	Spectral resolution (Å)	Range (Å)	Slit width (arcsec)	Spatial sampling (arcsec/pix)	Average seeing (arcsec)
ESO 96	1.5 m ESO	Jan. 1996	Boller & Chivens	0.98	1.86	5493–7505	2	0.78	1
LC 596	Dupont	May 1996	Boller & Chivens	1.0	1.10	6166–7190	1.25	0.56	1.5
LC 896		Aug. 1996		1.0	1.29	6149–7181	1.2	0.67	
LC 898		Aug. 1998		0.99	1.28	5540–7558	1.2	0.584	
WHT 96	WHT	Aug. 1996	ISIS	0.39	0.81	4757–5141	1.03	0.36	1.2
				″	″	6493–6880	″	″	″
				″	″	8505–8881	″	″	″
WHT 99		Dec. 1999	ISIS	0.44	0.92	3654–5187	1.03	0.20	1.5
				″	″	5354–6894	″	″	″
				0.39	0.81	8476–8872	″	0.36	″
WHT 00		May 2000	ISIS	0.44	0.92	3649–5185	1.00	0.20	1.3
				″	″	5334–6874	″	″	″
				0.39	0.81	8456–8852	″	0.36	″
CAHA 00	3.5 m CAHA	Jan. 2000	TWIN	0.38	0.80	4600–5380	1.20	0.56	1.2
				″	″	6240–7000	1.20	0.56	1.2

addition of the photon counting errors and of the errors on the continuum level determination.

We used cross-correlation techniques as described in Márquez & Moles (1996) to extract the gas kinematical information. The spatial section in the 2D spectrum with the highest S/N ratio (excluding the nuclear region for Seyferts[2]) was used as a template for the cross-correlation. The errors refer to the determination of the velocity shift with respect to the template spectrum. They are shown as error bars in the velocity distributions. For the stellar velocity distributions, the spectra in the CaT region were used, with cross-correlation techniques (as described in Pérez et al. 2000, and references therein), using as templates for the cross-correlation the observed spectra of several stars. The errors refer to the determination of the velocity shift with respect to the template spectrum. For clarity, error bars in the stellar velocity distributions are not plotted, but they typically amount to 50 km s^{-1}. The best S/N data have been used to look for the presence of nuclear dips in the stellar velocity dispersions, and are presented in Márquez et al. (2003).

The sample of active galaxies is more thoroughly observed (more PAs, higher S/N). Nevertheless, we do not expect this to produce a severe bias concerning general properties, since only the data along the major axes are used to characterize the rotation curves and use them to derive the Tully-Fisher (TF) relation, and to estimate the metallicity[3] of disk HII regions. With respect to the analysis of central structures, the same kind of S-shaped deviations seems to be present along all major axes.

[2] Notice that in the nuclear regions of AGNs there are often several components, which we have not attempted to fit individually.

[3] As given by [NII]/Hα, see below.

Besides, for a number of galaxies (most of them active spirals), enough position angles have been observed and therefore a guess can be made on what specific feature (disk or bar) may be the origin of such deviations (see below).

3. The shape of the rotation curves

The gas velocity distributions measured along various slit position angles for all the galaxies of our sample are displayed in Figs. 2 to 51, with the exception of NGC 2811 for which the [NII] emission lines are not spatially extended, and were detected in the nuclear region only (Hα is not detected in emission). The kinematical center and systemic velocities were determined as in Márquez et al. (2002): the kinematical center was defined as the cross section leading to symmetrical differences between the two horizontal branches of the rotation curve. That center corresponds, within our resolution, to the photometric center, i.e., the maximum in the continuum distribution along the slit, the biggest differences in position always being smaller than 2 pixels. The redshift corresponding to that kinematical center was adopted as the redshift of the system.

The stellar velocity distribution, when available, is shown superimposed on the gas data. Model rotation curves that better account for the observed data are shown in the figures as full lines; a normalized arctangent rotation curve function has been used, $v(R) = v_0 + \frac{2}{\pi} v_c \arctan(R)$, with $R = (r - r_0)/r_t$, where v_0 is the velocity of the center of rotation, r_0 is the spatial center of the galaxy, v_c is the asymptotic velocity and r_t is a radius that corresponds to the transition region between the rising and the flat parts of the rotation curve (see Márquez et al. 2002). Their

Table 4. Parameters derived from the velocity distributions along the major axes.

Galaxy	i	D_{25}	PA_{maj}^{RC3}	PA_{maj}^{kine}	r_G	v_G	r_1	v_1	r_m	v_m	cz	r_0	v_0
					($''$)	(km s^{-1})	($''$)	(km s^{-1})	($''$)	(km s^{-1})	(km s^{-1})	($''$)	(km s^{-1})
	(1)	(2)	(3)	(4)	(5)	(6)	(7)	(8)	(9)	(10)	(11)	(12)	(13)
UGC 1395	0.10	1.10	–	165	1.79	29	8.8	78	34	140	5139	4.5	132
IC 184	0.31	1.02	7	7	0.54	114	9.0	127	28	163	5332	0.5	120
IC 1816	0.07	1.16	–	150			3.0	177	21	159	5095	1.5	130
UGC 3223	0.25	1.15	80	68	0.80	77	1.6	111	21	250	4330	4.5	158
NGC 2639	0.22	1.26	140	135			6.0	229	33	310	3177	5.5	291
IC 2510	0.27	1.10	148	148			12.0	110	27	130	2529	7.5	119
NGC 3660	0.09	1.43	115	115	1.50	50	19.0	110	64	130	3441	4.5	155
NGC 4507	0.10	1.22	–	65	2.10	174	5.0	240	36	220	3689	1.5	130
NGC 4785	0.31	1.29	81	81	0.93	123	8.9	254	50	257	3672	1.5	197
NGC 5347	0.10	1.23	130	130?	–	–	–	–	–	–	2382	–	–
NGC 5728	0.24	1.49	0	0	0.30	85	5.0	194	56	189	2813	1.5	180
ESO139-12	0.11	1.20	35	15			10.0	218	114	252	5139	5.5	180
NGC 6814	0.03	1.48	–	–	–	–	–	–	–	–	1556	–	–
NGC 6860	0.25	1.13	34	34	0.98	38	10.0	184	40	190	4437	3.0	157
NGC 6890	0.10	1.19	152	152	1.70	55	6.0	120	54	124	2528	2.5	148
NGC 6951	0.08	1.59	170	170			7.5	145	96	153	1414	2.0	130
NGC 151	0.34	1.57	75	75	0.90	78	7.5	280	100	227	3727	1.5	170
NGC 1357	0.16	1.45	85	–			5.5	160	55	137	2033	2.5	115
IC 454	0.28	1.24	140	140	0.40	48	16.0	227	44	228	3973	3.5	155
NGC 2712**	0.26	1.46	178	–	2.5	106	20	150	49	152	1833	1.5	115
NGC 2811	0.46	1.40	20	–	–	–	–	–	–	–	2514	–	–
NGC 3571	0.46	1.48	94	–	0.90	85	2.0	143	26	153	3771	0.8	106
NGC 3835**	0.39	1.29	60	–	0.90	32	25	190	48	198	2452	6.5	150
NGC 4162**	0.22	1.37	174	–	1.3	61	22	159	48	160	2542	2.5	130
NGC 4290**	0.16	1.37	90	–	0.80	35	11	180	31	180	3035	3.5	145
NGC 6012	0.14	1.32	150	168	–	–	13.6	99	64	111	1988	8.2	150
NGC 6155**	0.16	1.13	145	–	1.5	30	12	80	41	90	2429	5.5	95
NGC 7328	0.44	1.31	88	88	2.0	73	8.0	150	77	150	2793	2.0	107

(1) and (2) inclination and isophotal diameter, respectively, as given in RC3 (in its units); (3) major axis position angle as given in RC3; (4) kinematical major axis as determined from our data; (5) distance to the center of the point out to which the solid body rotation is seen; (6) the velocity measured at r_G; (7) distance to the center of the point where the first maximum peak in velocity; (8) the velocity measured at r_1; (9) maximum distance to the center in the velocity distribution; (10) the velocity measured at r_m; (11) systemic redshift as measured from our data; (12) and (13) parameters for the model rotation curve (see text).

* Taken from NED.
** Excepting the last two columns, the values are from Márquez et al. (1996).

corresponding parameters are given in Table 4. These do not correspond to best fits, but only to the models which by eye fit best the data points along the various PA, with priority given to the major axis. This model has been used for the sake of comparison with Márquez et al. (2002, hereafter M111) and is quite appropriate to describe the general shape of the rotation curves of spiral galaxies, in particular concerning the parameters used for Tully-Fisher studies (Courteau 1997; M111 and references therein). These models are also used to constrain the kinematical major axes, for which the use of a more refined mathematical form is not critical. In two cases (UGC 3223 and ESO 139-12) the kinematical major axis is found to be
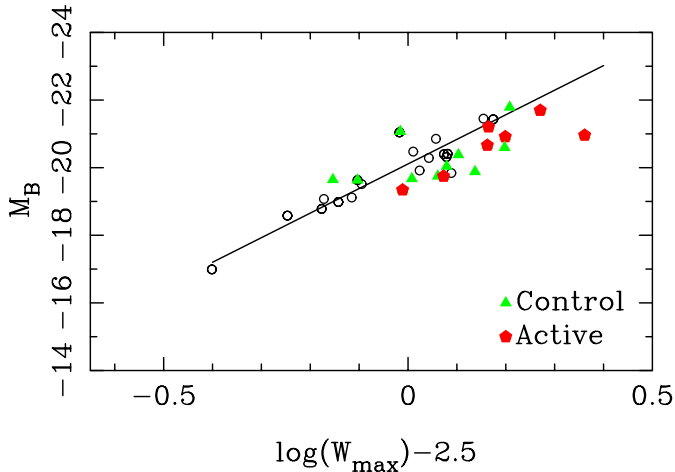
Fig. 1. Tully-Fisher relation for the galaxies of our sample (pentagons for active galaxies and triangles for non-active ones), together with the isolated galaxies of the M111 sample (empty circles). M_B is the B corrected absolute magnitude, and $W_{max} = 2 \times V_{max}(\mathrm{km\,s^{-1}})$ is the total amplitude of the rotation curve. The line indicates the TF relation by Tully & Pierce (2000).

different from the photometric major axis (taken from the RC3 catalogue). For UGC 1395, IC 1186 and NGC 4507, no photometric PA is given in the RC3 (see Table 4 for the major axis PA derived from our kinematical data). In a number of cases the number of slit positions and data points were not sufficient to obtain a full kinematical model (see below).

To check whether the galaxies of the DEGAS sample obey the Tully-Fisher (TF) relation, we plot in Fig. 1 the absolute magnitude B_{T0} (obtained from the corrected B magnitude given in the RC3) as a function of the rotation amplitude. The latter was estimated at $R_{opt} \approx 1.2 \times R_{25}$. The extrapolation of the model curve was used to get $V_{opt} = V(R_{opt})$, as in M111. It is clear from the figure that active and control galaxies populate the same area of the TF plane, indicating that their overall kinematical properties are similar. The small offset along the x-axis indicates that, within 1σ, Seyfert galaxies have median rotation velocities higher that control galaxies, for the same median luminosity. We also see that they are defining, within 1σ, the same TF relation as the isolated galaxies discussed in M111 (the DEGAS sample comprises earlier spirals, that tend to be more luminous and therefore are expected to be placed in the upper region of the diagram). We notice however that, even within 1σ, most of the active and control galaxies discussed here are located below the TF line defined in M111. The reason could be the differences in morphological content between the samples in M111 and here, or the need for more accurate absolute magnitudes than those provided by the RC3. Indeed, it also could be just an artifact of the small number statistics.

We give below details on the velocity curves of each galaxy with indications of particular aspects such as departures from the general rotation curve or differences between the gas and star velocity distributions. Most galaxies of our sample show rotation curves in global agreement with circular motions, but including some interesting details. S-shape structures are quite common near the nuclear regions, sometimes with different

amplitudes on either side, and often showing a velocity dip along the minor axis. To better see the behaviour of such departures, the model rotation curve has been subtracted from the data for each PA and the corresponding residuals have been inspected. In fact, zero velocity residuals are expected along the major axis when the inner disk axis has the same major axis than the large scale one; a rotation-like sinusoidal feature is expected when these two axes are misaligned, with amplitudes differing for the different PAs. This allows hence a better discrimination between nuclear bar or nuclear disk as the origin of such S-shape features, although for a definitive conclusion integral field spectroscopy is required. The departure from simple rotation explained for some galaxies by the presence of a bar and/or of a spiral arm are usually also based on our previously published optical (Márquez & Moles 1996) or infrared (Márquez et al. 1999) images.

3.1. Active galaxies

UGC 1395 (Fig. 2) has a rather smooth rotation curve. Only at PA = 45° and 135° the observed velocity distribution slightly departs from the overall rotation pattern. There is no entry for the photometric major axis in the RC3. Our data indicate that the kinematical major axis is at PA $\simeq$ 165°. The gas and stellar rotation curves look pretty similar along PA = 80° and 125°; but along PA = 35° the stars follow very well the model ±3 arcsec from the nucleus, whereas the gas velocity distribution deviates from this curve by about 30 km s^{-1} 2 arcsec NE of the nucleus (see also Fig. 3). This occurs at the position of the bent dust lane structure originating at the NE extremity of the nuclear bar (Pogge & Martini 2002). The residual velocity plots[4] indicate that the S-shape structure interior to ±5 arcsec, more clearly visible along PA = 125° and PA = 35°, may originate in the inner bar structure (see Fig. 3).

The kinematical and photometric major axes in IC 184 are coincident. The gas (Fig. 4) shows a strong asymmetric departure from the model rotation curve, specially along PA = 7° and 97° (major and minor axis, respectively) out to ±10 arcsec from the center, while the stellar velocities follow quite well the model along PA = 97° (the stellar velocity distribution along PA = 7° is given in Márquez et al. 2003). This is illustrated in the enlarged figure of the central zone along PA = 97° and in Fig. 1 of Márquez et al. (2003). For the gas, the $\approx$100 km s^{-1} difference between the data points and the rotation model N and NE of the nucleus along PA = 7° and 37° are most probably due to the bar and north spiral arm; the bump observed along PA = 97° is most probably also due to the bar. Note that a drop in the stellar velocity dispersion is observed in this galaxy (Márquez et al. 2003). The residuals of the gas velocity distributions along PA = 37° and PA = 157° in the inner ±1 arcsec (see Fig. 5) hint for the presence of a nuclear disk, as those found in some active galaxies (see Márquez et al. 2003 and references therein). Although IC 184 has been selected as an isolated spiral following the criteria defined for the DEGAS sample, we recently came upon a paper indicating that it has several
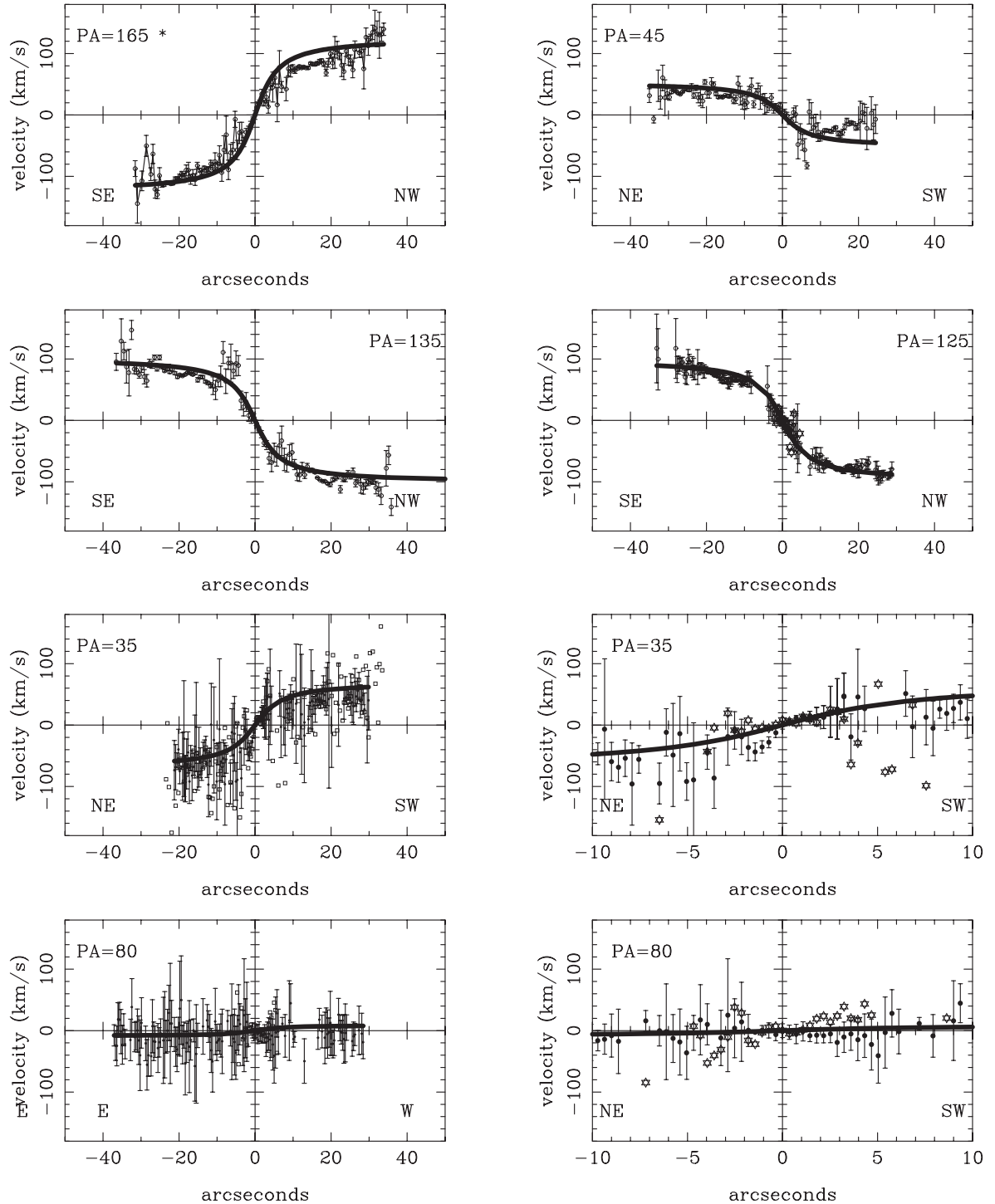
---

[4] Available in electronic form only.

UGC 1395

Fig. 2. Velocity distributions for UGC 1395. As for all similar figures, gas velocities derived from Hα and Hβ are shown as black dots (with error bars) and empty light circles respectively. Stellar velocities are shown with stars. For PA = 35 and 80° an enlarged part of the central region is plotted to see better the corresponding stellar kinematics. An asterisk after the PA indicates the slit position angle coinciding with the major axis. The line corresponds to the rotation model which best reproduces the data.

spectroscopically confirmed faint companions (Kollatschny & Fricke 1987).

The ionized gas in IC 1816 (Fig. 6) presents a rather smooth velocity distribution along the two perpendicular PAs. Our data

indicate that the kinematical major axis is at PA ≃ 150°. No value is given in the RC3 for the photometric major axis. The measured velocities north of the nucleus along PA = 0° are about 50 km s^{-1} higher than expected, probably due to the

IC 184
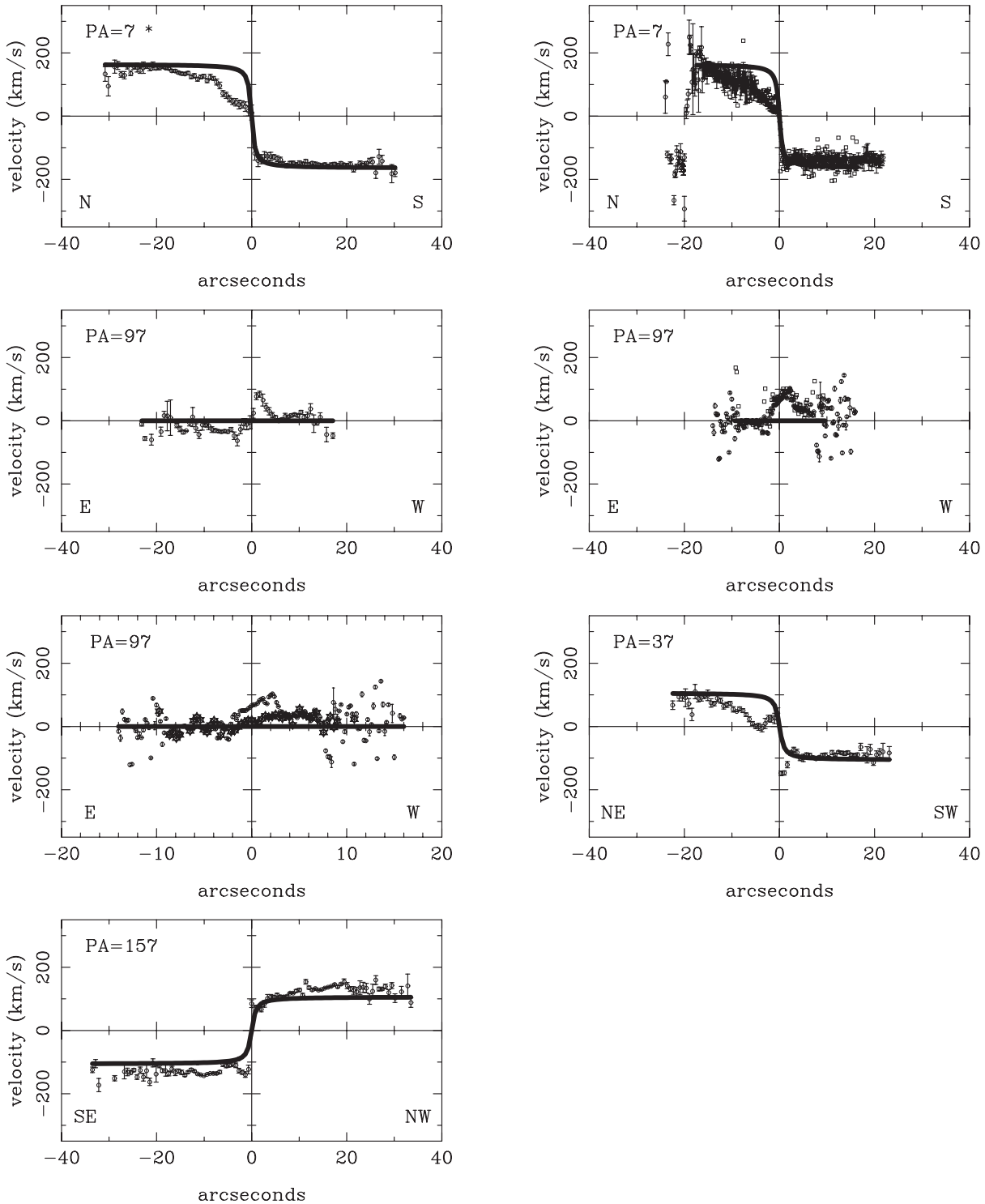
Fig. 4. Velocity distributions for IC 184. The two sets of two curves along PA = 7 and PA = 97 correspond to the LC (left) and WHT (right) data. An enlarged part of the central zone is shown with stars indicating the stellar component.

presence of a spiral arm. The small counter-rotation observed roughly ±3 arcsec from the nucleus could be due to the presence of the inner bar, but it could also trace the presence of a nuclear disk (see Fig. 7).

UGC 3223 (Fig. 8) presents a rather smooth gas velocity distribution with a major axis in better agreement with PA ≃ 70° than with the photometric major axis given in the RC3 (PA = 80°). An S-shaped structure is also visible in this galaxy,
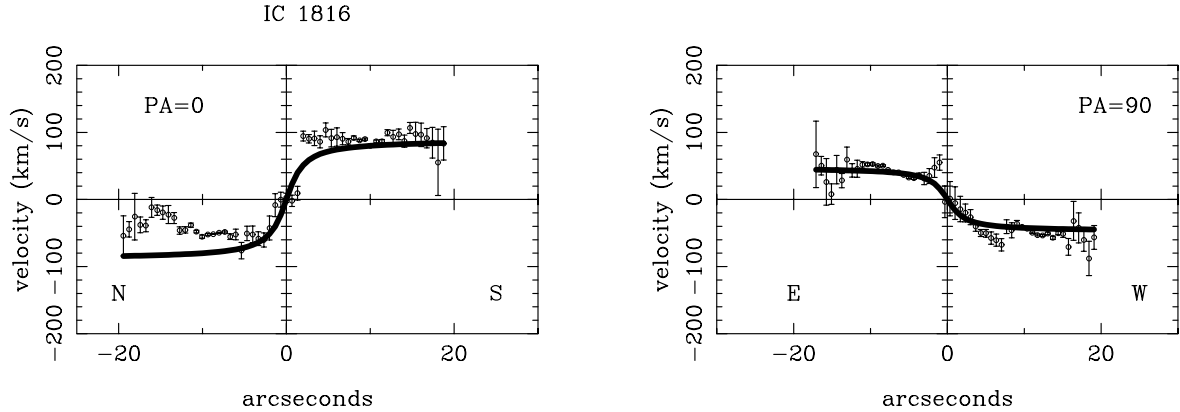
IC 1816

Fig. 6. Velocity distributions for IC 1816.

specially along PA = 20° and also along PA = 170° (close to the kinematical minor axis) where it is asymmetric in amplitude. The stellar and gas velocity curves in the central region along PA = 80° are given in Fig. 2 of Márquez et al. (2003), where the presence of a drop in the stellar velocity dispersion is reported. An S-shape structure at ±4 arcsec in the residuals, observed in all position angles but more clearly visible at PA = 20°, can be attributed to the inner bar (see Fig. 9).

NGC 2639 (Fig. 10) shows smooth gas and star rotations along the three PA for which we have data. Along PA = 135° (the photometric major axis is at PA = 140°), the stars follow the model throughout while the gas shows some wiggles (see Fig. 11). Along PA = 0°, the gas and stellar velocities follow each other, with an apparent counter-rotation in the innermost ±1 arcsec, which is also visible for the gas along PA = 45°. The counter-rotation is more clearly evidenced in the residuals, which show that it is also present along PA = 135° (see Fig. 11). The rotation curves are given for the gas and stars along PA = 45° in Márquez et al. (2003), where the presence both of a nuclear disk from HST images and of a drop in the stellar velocity dispersion are discussed. The residuals in the inner ±2 arcsec seem to be due to the inner bar.

IC 2510 (Fig. 12) shows rather smooth gas rotation, with small deviations about 5–12 arcsec SE of the nucleus along PA = 148° and 8–15 arcsec NW of the nucleus along PA = 118°, both probably due to the presence of a bar. A small asymmetric S-shape structure is present in the central ±3 arcsec, more clearly detected at position angles other than the major axis in Fig. 12, and along all the PA in the residuals (see Fig. 13). This structure coincides with a region immediately SW of the major axis, which is an incomplete arc-like structure visible in the HST image. The global shape of the rotation curve along the major axis agrees with that given by Persic & Salucci (1995).

NGC 3660 (Fig. 14), for which the kinematical and photometric major axes coincide, shows a stellar rotation pattern that is well fit by the rotation model along PA = 115°. The velocity distribution of the gas shows a bump of about 100 km s^{-1} in the region between 3 and 5″ to the NW of the center, with residuals around zero for PA = 145° (see Fig. 15); this could indicate the presence of a nuclear disk perpendicular to this PA. A possible stellar counter-rotation is seen in the inner ±1 arcsec along

PA = 85°, but the stellar data for this PA are very noisy and no firm conclusion can be extracted. The outer parts of the rotation curve of the gas are not well accounted for by the model, probably due to the crossing of various spiral arms.

For NGC 4507 (Fig. 16) we estimate a kinematical major axis at PA ~ 65° (no value is given in the RC3 for the photometric axis). The gas velocity distribution along PA = 51° is in general well represented by the model, but it is somewhat wiggly along PA = 141°, where it shows an asymmetric S-shape structure with a strong dip (about 100 km s^{-1}) between 2 and 10 arcsec SE of the nucleus (see Fig. 17).

NGC 4785 (Fig. 18) shows a smooth rotation pattern for the gas along PA = 81° (the major axis), with a velocity drop about 8 arcsec W of the nucleus, probably due to the bar and/or beginning of the spiral arm; the velocity field has a number of wiggles along PA = 171°, with an S-shape structure in the inner ±10 arcsec, deeper to the South (see Fig. 19); no obvious morphological feature is seen in this region in our infrared image.

NGC 5347 (Fig. 20) has too sparse data to be analyzed in detail. Notice however that an apparent counter rotation is noticed in the central ±5 arcsec along both the photometric major (PA = 130°) and minor (PA = 40°) axes (see the inset shown in Fig. 21). This region coincides with the dust lane seen in the HST map (Pogge & Martini 2002).

For NGC 5728 (Fig. 22), the photometric and kinematical major axes are in excellent agreement (PA = 0°). The gas kinematics show strong departures from the expected, standard disk rotation model along the four observed PA. The velocity gradient is very steep in the few arcseconds around the nucleus. Our data are in agreement with the previous determination by Schommer et al. (1988), who derived a position angle for the major axis at 2 ± 5°. Our better spatial resolution allows us to detect a strong velocity discontinuity a few arcseconds on either side of the nucleus which is seen along PA = 90° (corresponding to the minor axis) and PA = 150° in Fig. 22 and along all the PAs in the residuals (see Fig. 23). These position angles are close to those used by Emsellem et al. (2001) to derive stellar velocity distributions within the central ±5 arcsec; the resulting stellar kinematics are very smooth, and show no velocity discontinuity. This seems to show evidence for a massive central gaseous disk, decoupled from the stars, somewhat similar to the one we found in NGC 6951 (Pérez et al. 2000).
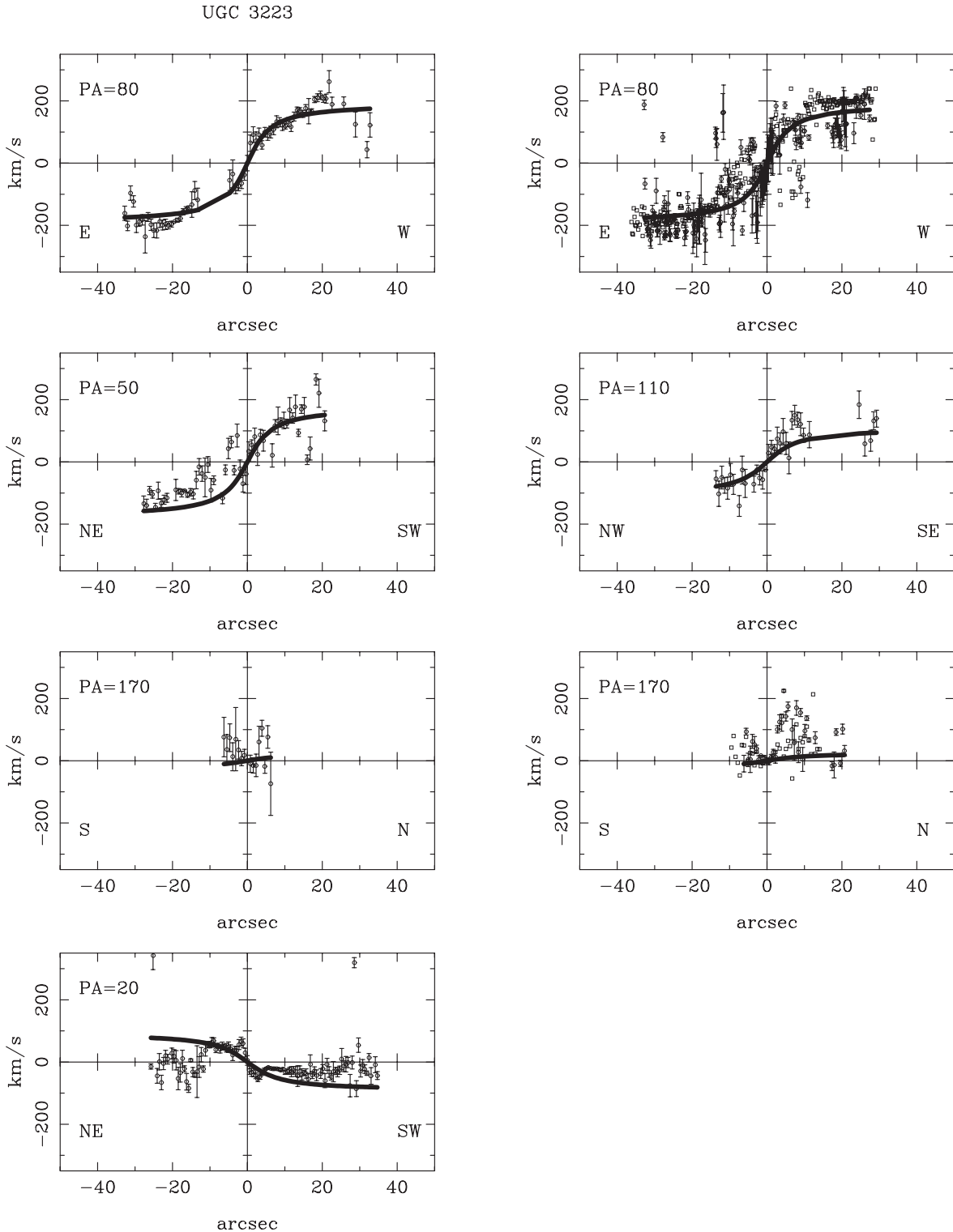
UGC 3223

Fig. 8. Velocity distributions for UGC 3223. The two sets of curves along PA = 80° and PA = 170° correspond to 4m class telescopes (right) and ESO (left) data.

However, the presence of two components within the inner ±10 arcsec detected with a higher spectral resolution by Prada & Gutiérrez (1999) could have an influence on the shapes of the rotation curves.

ESO 139-12 (Fig. 24) appears to be the only unbarred galaxy in our subsample of active galaxies, even after analysis of the infrared images (Márquez et al. 1999, 2000) and shows smooth rotation along all observed PA. The differences

NGC 2639
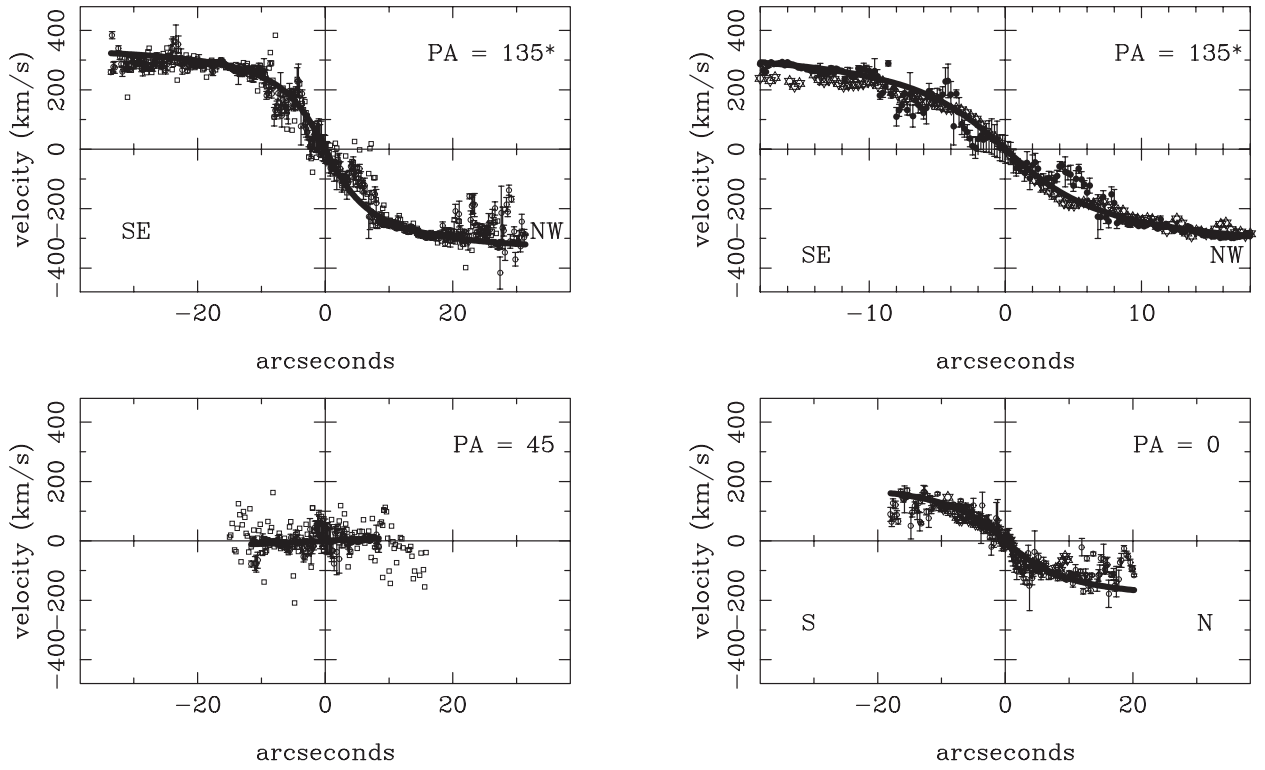
Fig. 10. Velocity distributions for NGC 2639. The top right figure shows an enlargement of the central region with the stellar velocities indicated in blue.

IC 2510
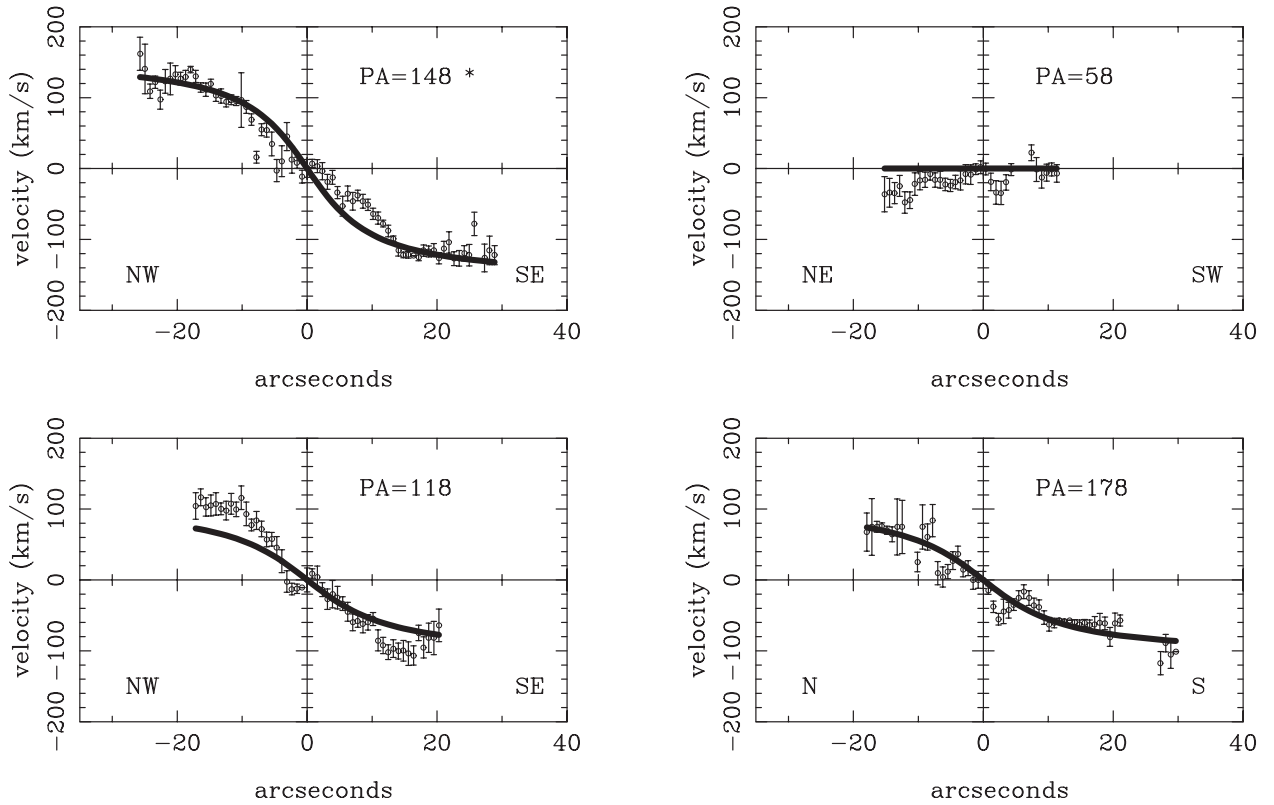
Fig. 12. Velocity distributions for IC 2510.

NGC 3660
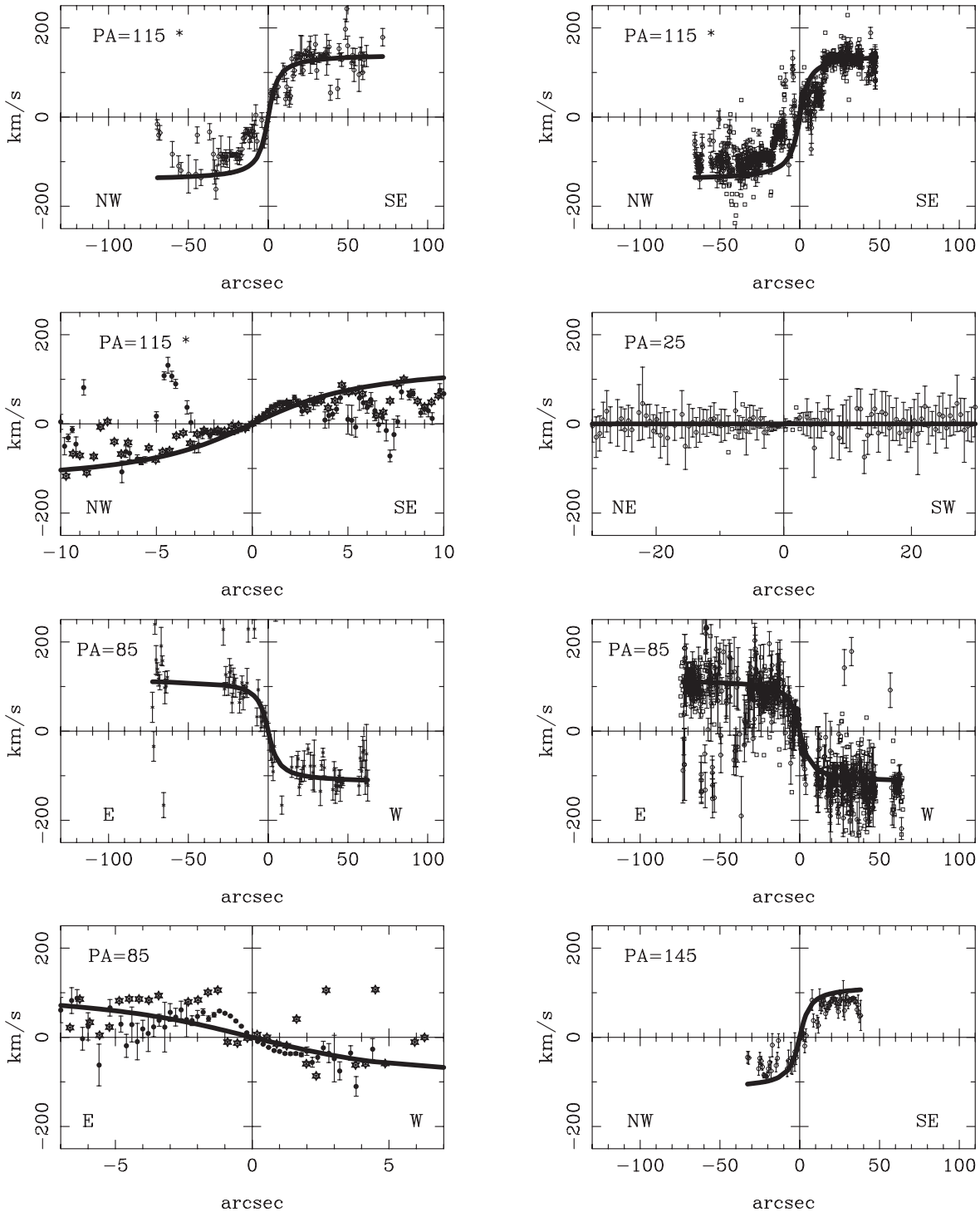
Fig. 14. Velocity distributions for NGC 3660. The ESO96 (left) and WHT99 (right) curves are on the top line for PA = 115. A zoom of the central region of the WHT99 data along PA = 115 is shown in the second line, together with the curve along PA = 25 where a few velocities from the Hβ line are visible in the very center. The ESO96 (left) and WHT99 (right) curves are on the third line for PA = 85. A zoom of the central region of the WHT00 data along PA = 85 is shown in the fourth line.

between the model and the observed gas kinematics are minimized when the kinematical major axis is placed at PA = 15°, instead of 35° as given in the RC3 for the photometric axis. An S-shape structure is detected in the inner few arcseconds,

specially visible along PA = 120° and 125°. This could correspond to an incomplete spiral-like feature detected in the innermost 1″.8 in the HST image. The residuals indicate that this
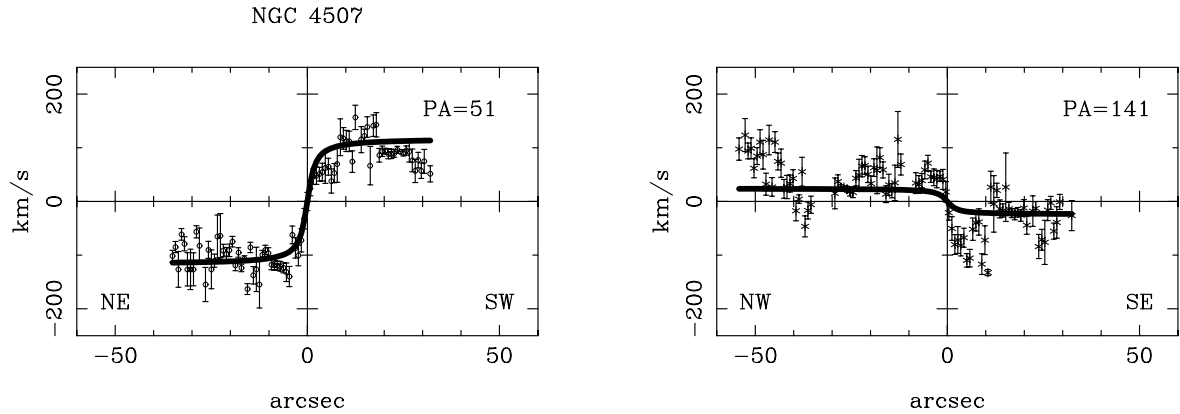
NGC 4507

Fig. 16. Velocity distributions for NGC 4507.
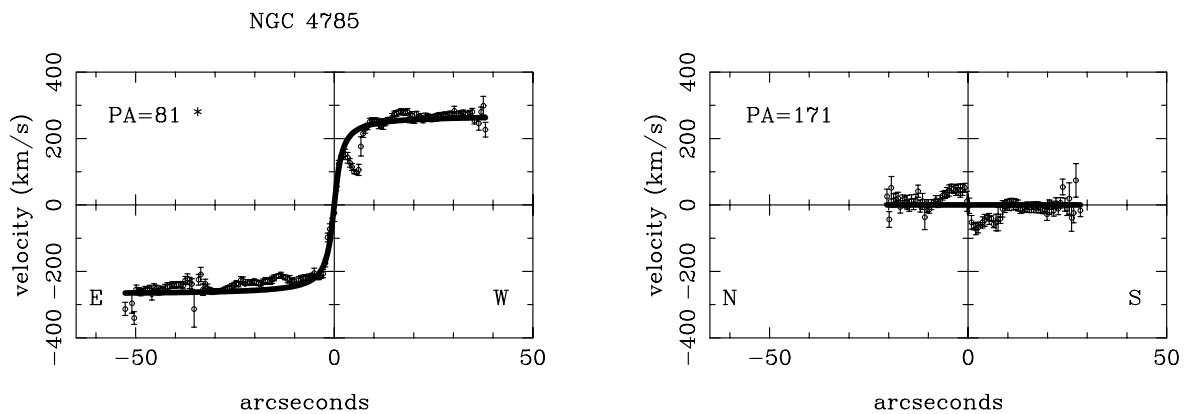
NGC 4785

Fig. 18. Velocity distributions for NGC 4785.
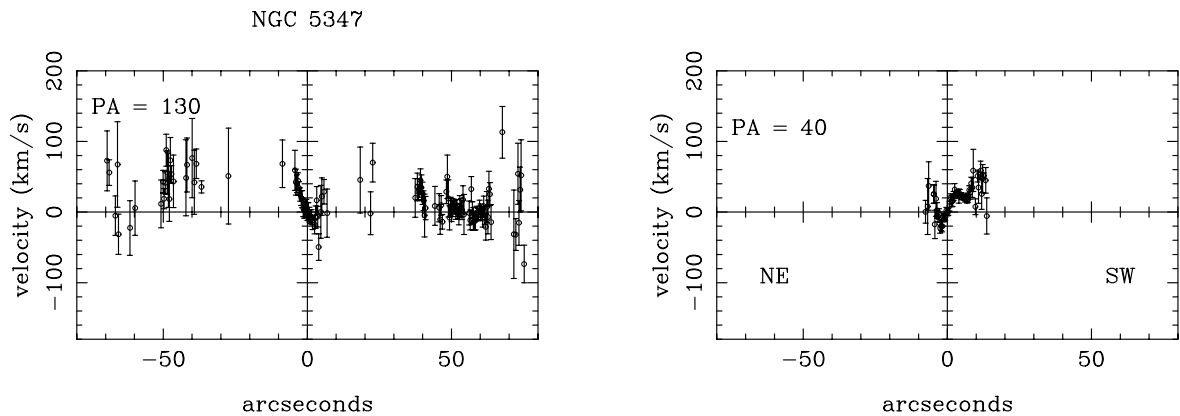
NGC 5347

Fig. 20. Velocity distributions for NGC 5347.

feature may be produced by a nuclear disk with a minor axis close to PA = 60–65° (see Fig. 25).

NGC 6814 (Fig. 26) is seen too close to face-on for any kinematical model to be applied. Note however that an asymmetric S-shaped structure in the gas velocities is observed in the central arcseconds of all the spectra, with a dominant northern component reaching maximum amplitude about 4 arcsec from the nucleus. This feature may be due to the presence of some structure within the bar, most probably also related to the drop detected in the stellar velocity dispersion (Márquez et al. 2003). Notice that the stars follow the gas along PA = 30° SW of the nucleus but not in the other direction. Stellar and gas rotation

curves along PA = 120° are also presented in Márquez et al. (2003), where the presence of a broad drop in the stellar velocity dispersion is discussed.

NGC 6860 (Fig. 27) has kinematical and photometric major axes in excellent agreement and shows smooth gas rotation along its major axis but a number of features, most probably due to the presence of the bar, are observed along the other PAs, such as an asymmetric S-like feature close to the nucleus, with departures from circular rotation up to 100 km s^{-1} along the minor axis (PA = 124°). The velocity gradient in the central region along PA = 64° (which crosses the bar) is steeper than expected from a simple rotation model. The residuals along the

NGC 5728
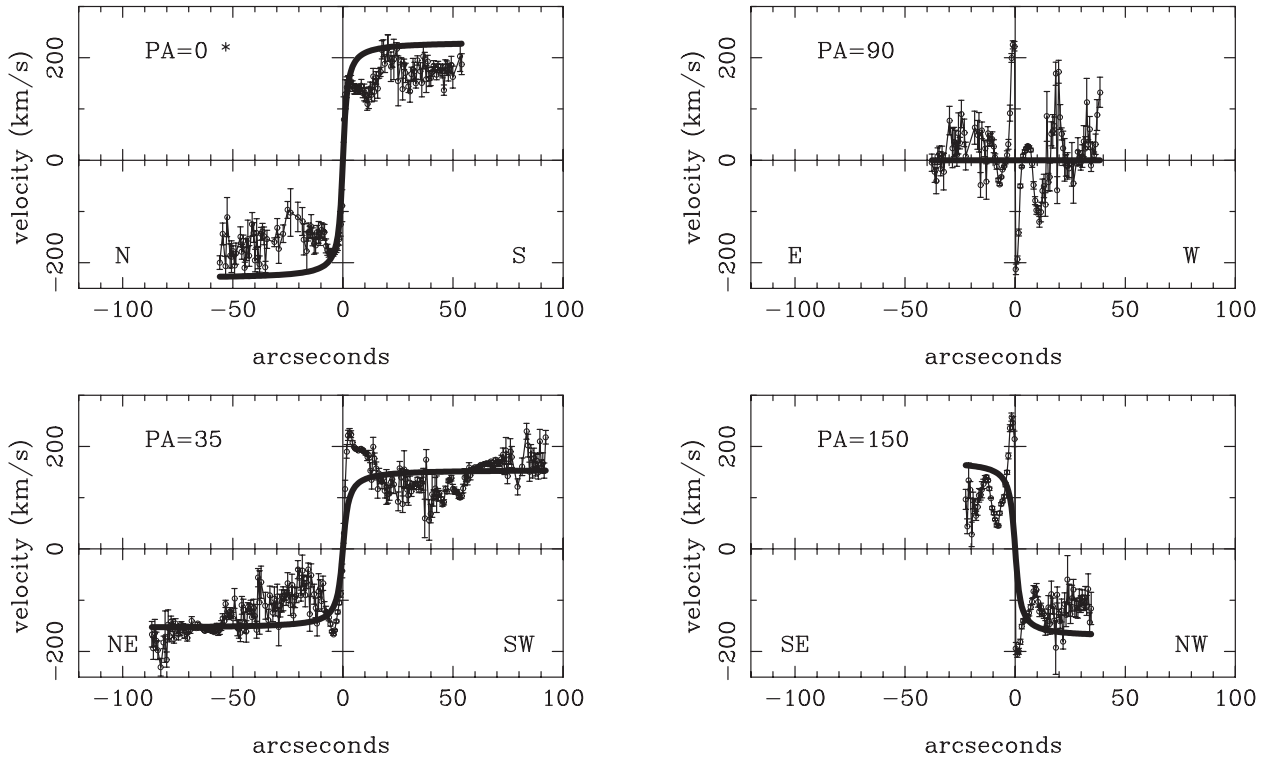
Fig. 22. Velocity distributions for NGC 5728.

observed PAs hint for the structure in these inner ±4 arcsec to be due to the inner bar (see Fig. 28).

NGC 6890 (Fig. 29) shows quite a regular circular gas rotation except along its minor axis (PA = 62°) where a wide velocity dip is observed NE of the nucleus, corresponding to one of the sides of an asymmetric S-like feature which is present along the other PAs (this is more clearly seen in the residuals, Fig. 30). The photometric and kinematical major axes are the same for this galaxy.

3.2. Non-active galaxies: New data

NGC 151 (Fig. 31) shows overall regular circular rotation along its major axis at PA = 75° (coincident with the photometric axis) but there are velocity dips along PA = 151° and 165° just NW of the nucleus. These dips correspond to an asymmetric S-shaped structure, with a maximum amplitude of almost ±200 km s^{-1} along PA = 151°, which is seen in the residuals for all the PAs (see Fig. 32). Such kinematical behavior could be created by a secondary bar 2″.5 long at PA = 68° visible in the HST image (see Fig. 34 in Márquez et al. 1999).

NGC 1357, an optically unbarred galaxy as classified in the RC3, shows an overall smooth gas rotation along PA = 85°, corresponding to the photometric major axis (Fig. 33). A S-like feature is visible mostly in the left side of the curve (see Fig. 34).

IC 454, for which we determine a kinematical major axis coincident with the photometric one (PA = 140° as in the RC3), shows somewhat wiggly gas rotation curves along all the four

observed PA (Fig. 35). An asymmetric S-like feature is also present in this galaxy, most clearly visible along PA = 110° in Fig. 35 but present in the residuals for all PAs (see Fig. 36). It produces a dip of about 100 km s^{-1} in the velocity distribution, SW of the nucleus along the minor axis (PA = 50°). The residuals seem to indicate that this feature is due to the nuclear bar.

NGC 2811 shows weak Hα in absorption and [NII] in emission in the very central region, and no emission lines further out, so it is not possible to analyze its kinematics.

NGC 3571 (Fig. 37) shows weak extended emission, only detectable along PA = 94° (its photometrical major axis) with an overall regular gas rotation. Departures from the model are too noisy to extract any conclusion (Fig. 38).

For NGC 6012 the best model (Fig. 39) requires the kinematical major axis to be at PA = 150°, as determined from near-infrared data (Márquez et al. 1999), whereas a value of PA = 168° is given in the RC3. The gas kinematics are compatible with overall circular rotation along PA = 168° except for a velocity drop about 30 arcsec S of the nucleus. However, the velocity distribution is less regular along PA = 78°, with an S-shape structure giving rise to a strong and broad dip 0−15 arcsec W of the nucleus. The residuals seem to hint for a nuclear disk as the origin of such motions (see Fig. 40). The simple rotation model used here does not account well for the data along this PA.

NGC 7328 (Fig. 41) shows regular circular gas rotation along the major axis (PA = 88°, both kinematical and photometric). Along the minor axis (PA = 178°) and at PA = 118° a

ESO 139
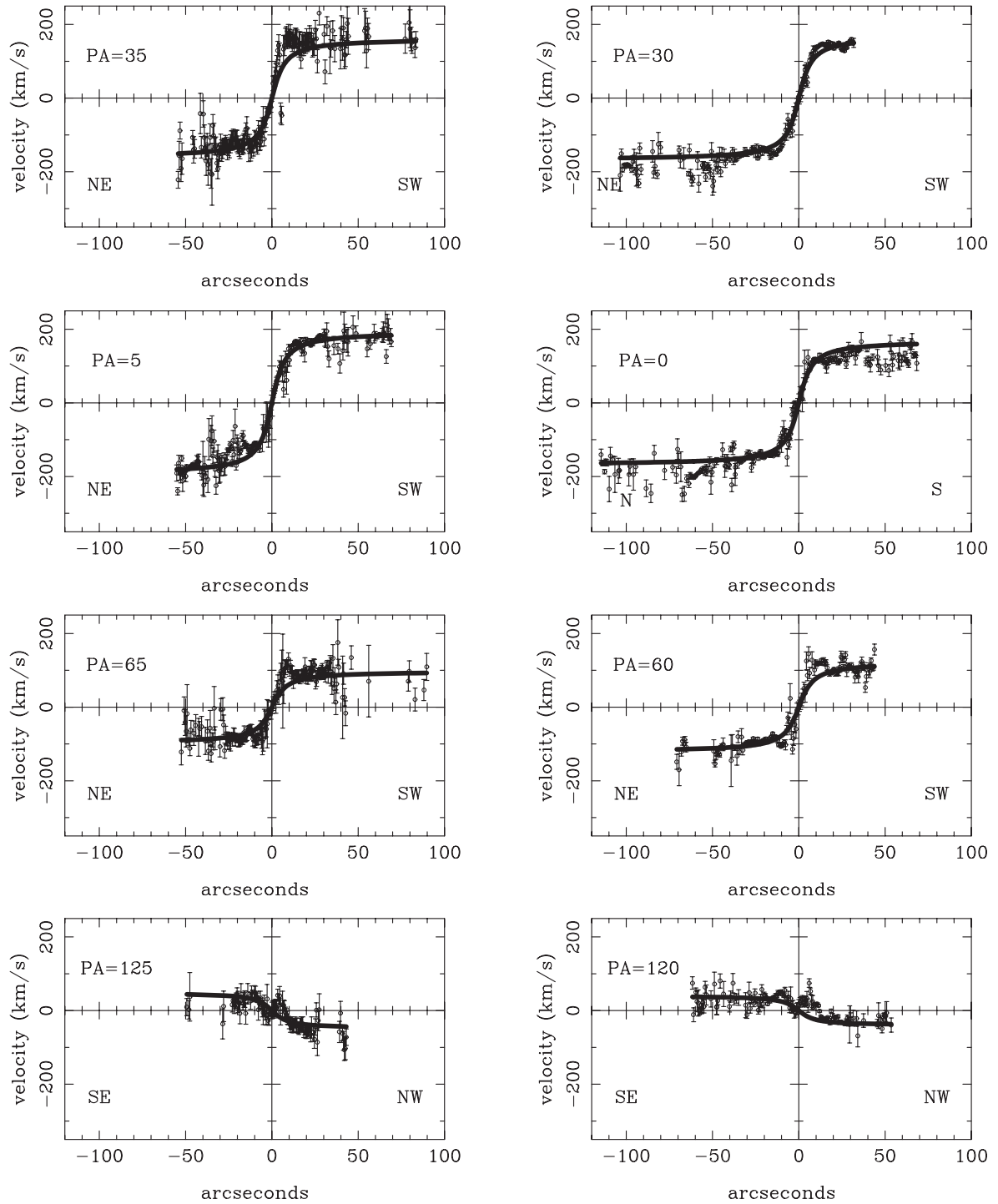
Fig. 24. Velocity distributions for ESO 139-12.

velocity dip is observed 0−12 arcsec N of the nucleus, corresponding to the most conspicuous side of an asymmetric S-like feature in the central ±10 arcsec. The inspection of the residuals favour the case of a nuclear disk with a minor axis close to 58° (see Fig. 42).

3.3. Non-active galaxies: Previous data

The gas kinematics of five galaxies from the DEGAS control sample have previously been observed along their major axis by Márquez & Moles (1996). These are: NGC 2712, NGC 3835, NGC 4162, NGC 4290 and NGC 6155. We made a

NGC 6814
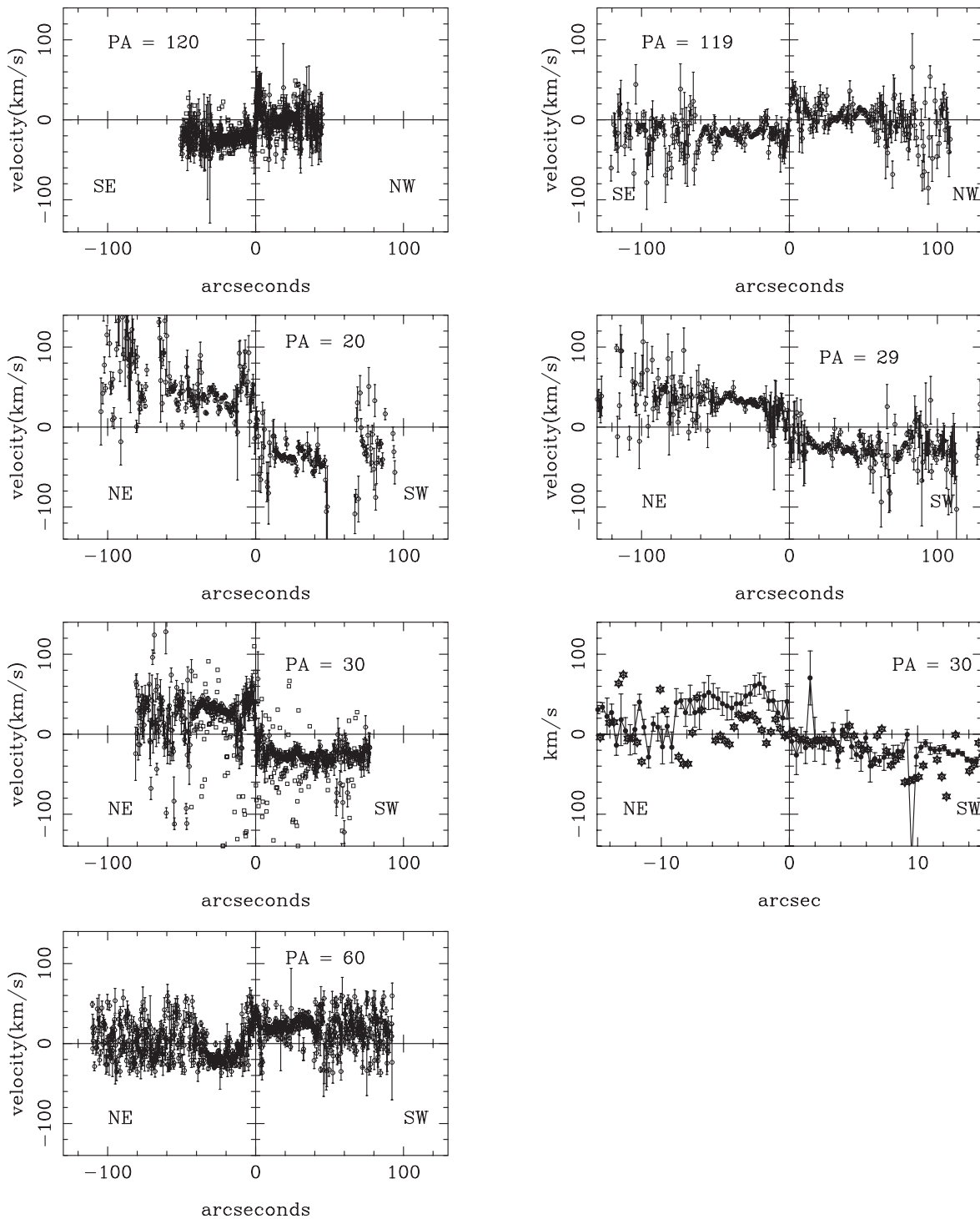
Fig. 26. Velocity distributions for NGC 6814. An enlargement of the central ±15 arcsec is given for PA = 30° with the stellar velocity distribution as stars.

rotation model similar to that described above and give the results for these five galaxies in Table 4. Their rotation curves are given in Figs. 43–51. For NGC 2712, the rotation curve agrees with that of Héraudeau & Simien (1998). The residuals with respect to the model are given in Figs. 44–52. In all of them evidences of the presence of S-shaped central structures can be seen.

NGC 6860
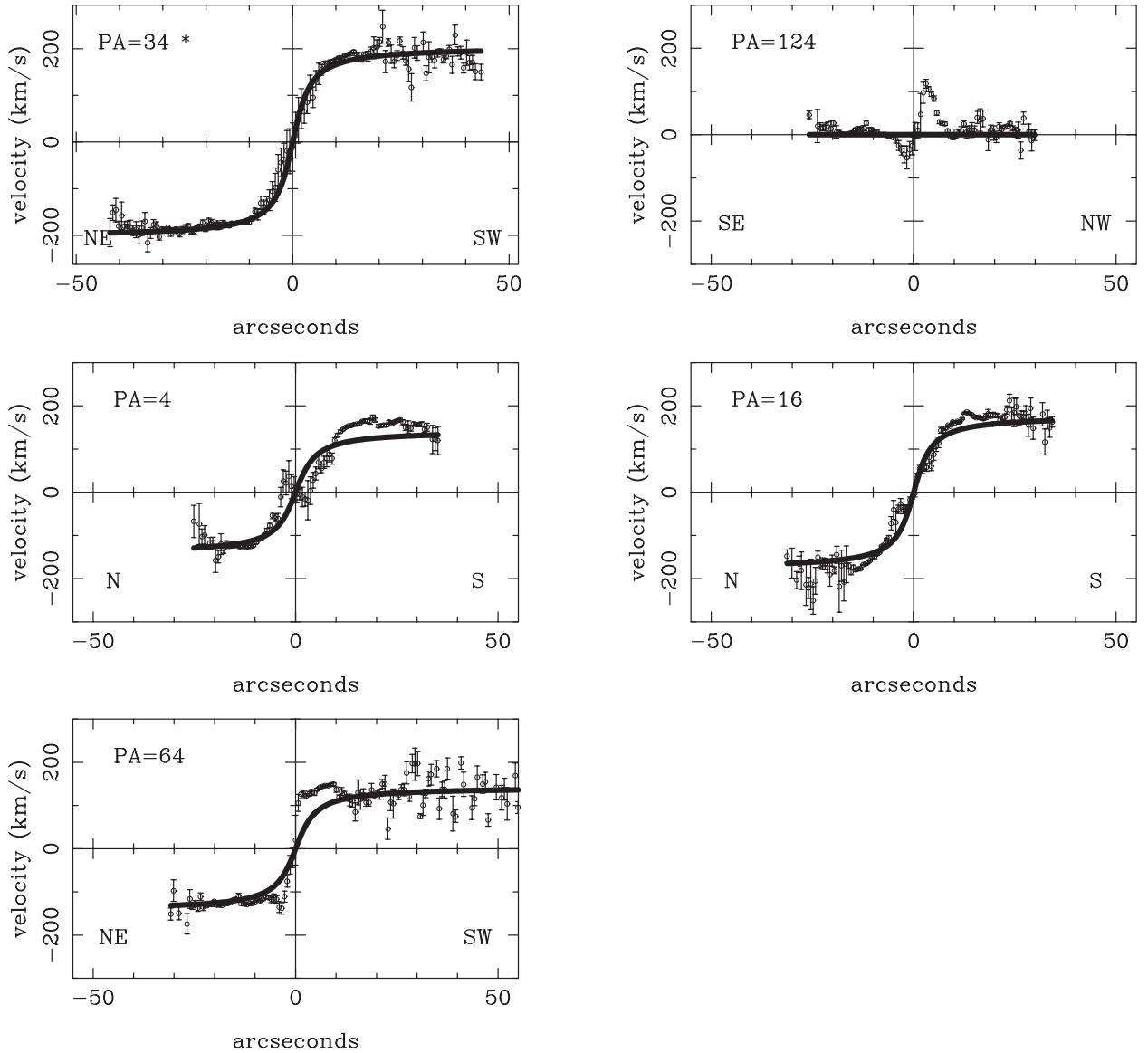
Fig. 27. Velocity distributions for NGC 6860.

4. Nuclear and disk spectral characteristics

The spectra for the different HII regions along the slit have been extracted and the emission lines measured as explained in M111, including only the 224 HII regions with $H\alpha$ equivalent widths larger than 10 Å (see below), and producing the data given in Table 5. This table is available in electronic form at the CDS via anonymous ftp to `cdsarc.u-strasbg.fr (130.79.128.5)` or via `http://cdsweb.u-strasbg.fr/cgi-bin/qcat?J/A+A/416/475`. The columns of this table are: 1. galaxy name; 2. slit position angle, anti-clockwise from north; 3. distance to the nucleus along the slit in arcsec; 4. $H\alpha$ equivalent width; 5 and 6. [OI]λ6300/$H\alpha$ line intensity ratio and corresponding error; 7 and 8. [NII]λ6584/$H\alpha$ intensity ratio and corresponding error; 9 and 10. [SII]λ6717+6731/$H\alpha$ intensity ratio and

corresponding error; 11. [SII]λ6717/[SII]λ6731 intensity ratio.

Plots of the nuclear spectra for all the galaxies of the DEGAS sample are displayed in Figs. 53a–c. The spectra of active nuclei in general agree with the AGN classification of the Véron-Cetty & Véron (2001) catalogue. Regarding the control galaxies, we find that 5 out of 12 have HII-like nuclei, a fraction that is lower than in M111. This could be due to the differences in morphological content between the two samples. We remember here that the control subsample was defined to match the morphological distribution of the active galaxies, which are preferentially seen in early type galaxies (Melnick et al. 1987). For the remaining 7 galaxies in the control sample, NGC 6012 has been previously classified as a LINER, and the others present a too strong $H\alpha$ absorption for a reliable classification. In any case, given the strength of the [NII] lines seen

NGC 6890
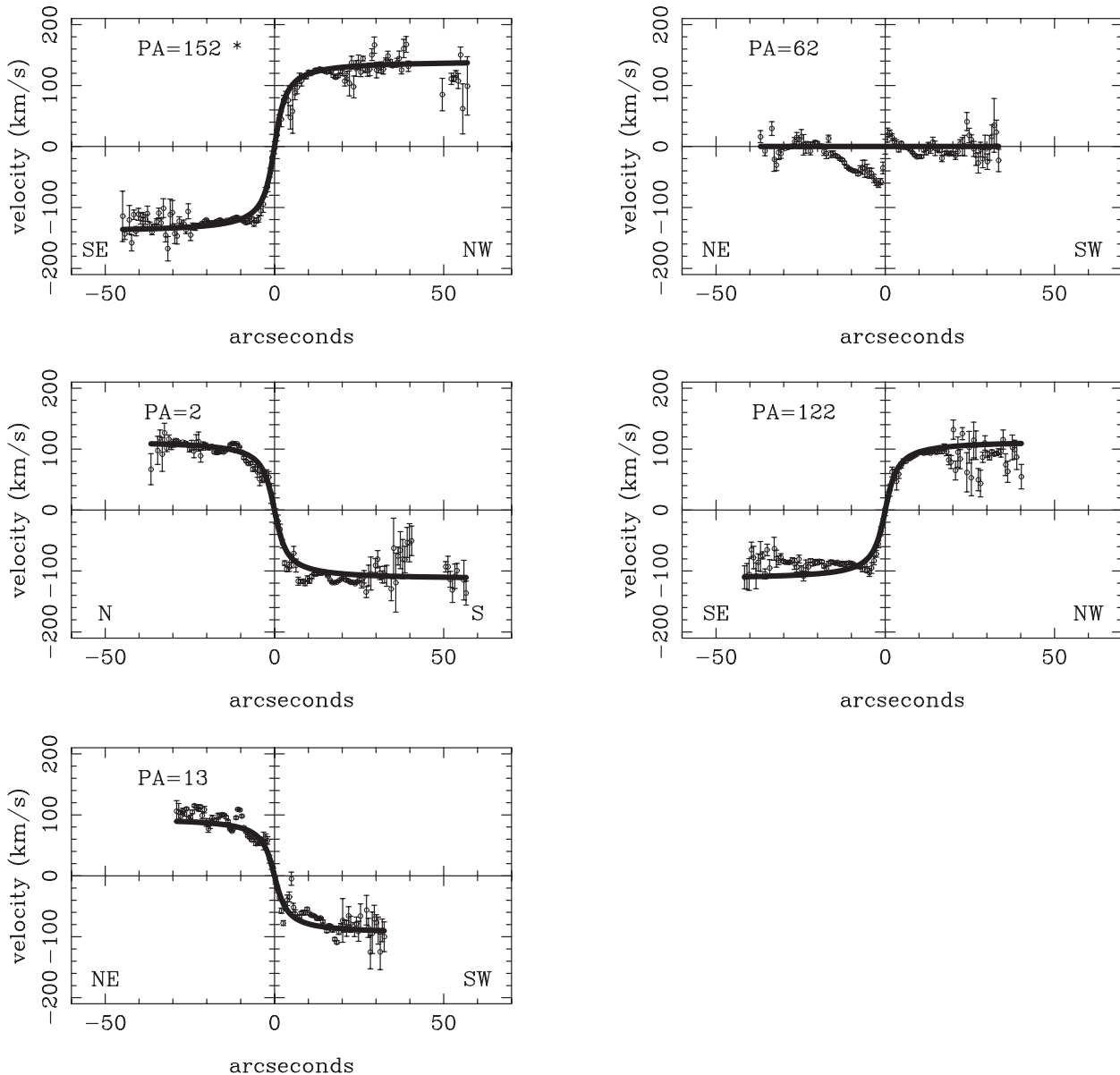
Fig. 29. Velocity distributions for NGC 6890.

in some nuclei, the possibility of some of them hosting dwarf-AGN nuclei cannot be discarded. Here too, the fact that most of the galaxies are early type spirals could be relevant since, as a matter of fact, a higher percentage of low AGN activity is expected for early type spiral galaxies (Ho et al. 1997).

An estimation of the metallicities of the disk HII regions and their possible gradients were obtained from the [NII]/Hα line ratios only. Denicoló et al. (2002) obtained an empirical calibration of the oxygen abundances based on this ratio, which they showed to be powerful when analyzing large survey data to rank their metallicities, but with quite large uncertainties on individual objects, mainly due to O/N abundance ratio and ionization degree variations. Here we only consider it to study global trends of Z from the spectra of HII regions

in our sample[5], along the same lines discussed in M111. The data don't allow us to conclude on each individual galaxy, but can be used to look for general trends when the population of the disk HII regions is considered as a whole. To be able to combine data from different galaxies, we have normalized the galactocentric distances of the HII regions to r_{25} (as given in the RC3)[6]. A plot of the [NII]/Hα ratios as a function of distance to the galaxy nucleus is displayed in Fig. 54 for the DEGAS sample, together with the values taken from the

---

[5] Note that we do not refer to the regions very close to the AGN in active galaxies.

[6] In the analysis we only include HII regions with Hα equivalent widths larger than 10 Å, as in M111. In that way we avoid including regions with strong Balmer absorption, that could induce inconsistencies in the estimation of the metallicity.
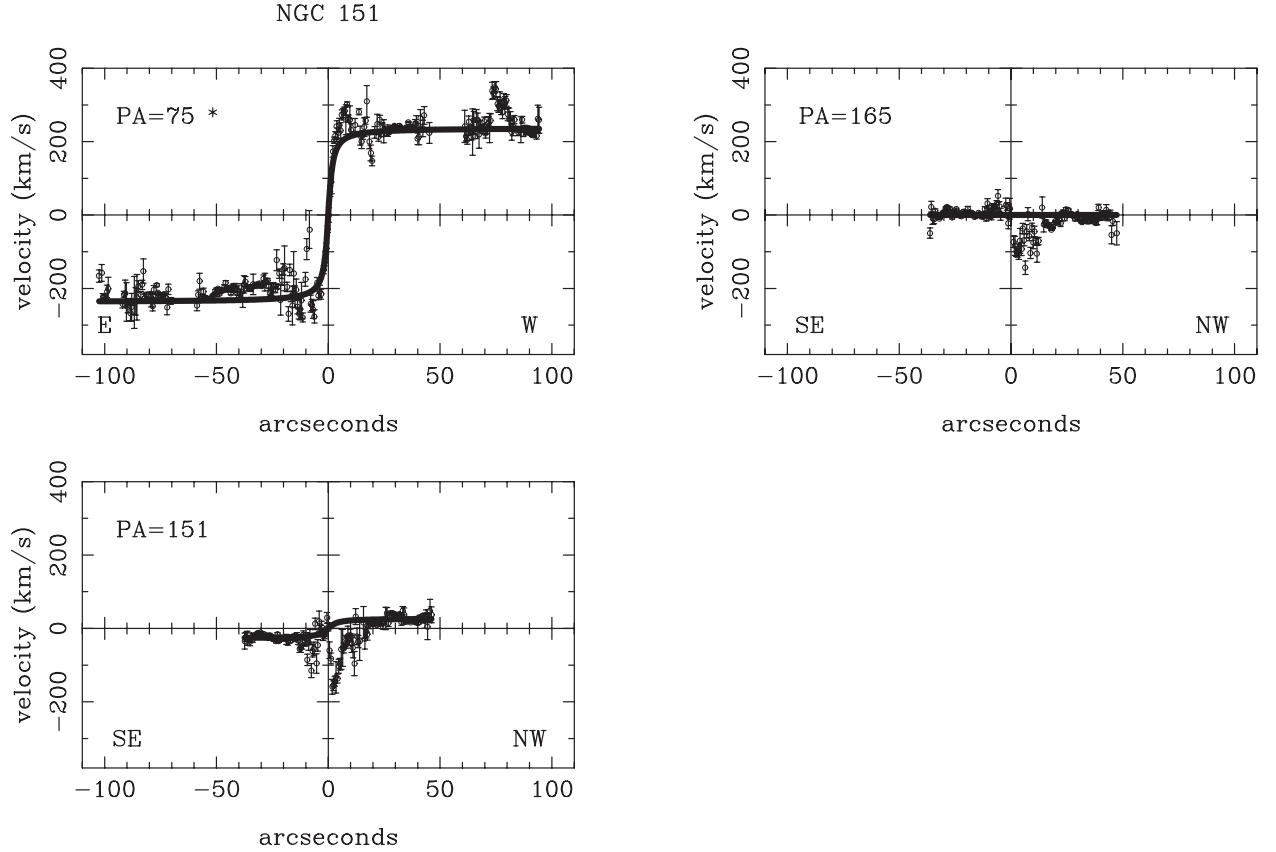
NGC 151

Fig. 31. Velocity distributions for NGC 151.
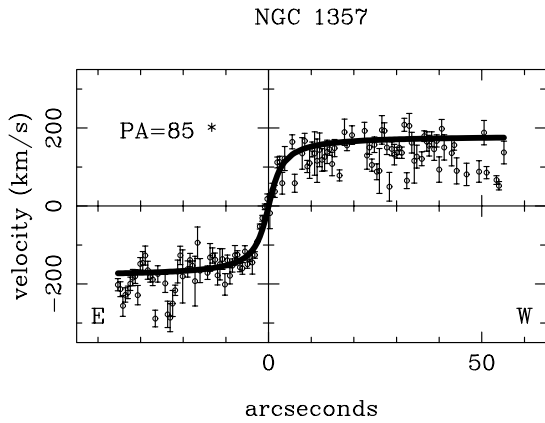
NGC 1357

Fig. 33. Velocity distribution for NGC 1357.

the differences are found only at a 1σ level: the median values are [NII]/Hα = 0.46 ± 0.07 for active galaxies and 0.39 ± 0.07 for non-active ones, to be compared with [NII]/Hα = 0.31 ± 0.07 for the isolated galaxies in M111 covering the same absolute magnitude range, i.e., M_B between −19 and −22.

We find that there is a deficiency of low [NII]/Hα values for the two DEGAS subsamples. If we now consider two families per subsample, early (Sa to Sb) and late (Sbc to Scd) spirals, we see that the deficiency is specially clear for late types. However, the DEGAS sample is obviously biased towards early type spirals in the case of active galaxies (see for instance Moles et al. 1995) and by construction for the control sample, and therefore no firm conclusions can be reached.

5. Summary and conclusions

We have presented and discussed the properties derived from the analysis of long slit spectra along several position angles of a sample of isolated active and non-active galaxies. A simple model has been used to trace overall rotation curve properties and obtain the parameters for Tully-Fisher (TF) analysis. The active and non-active spirals define very similar TF relations, populating the region occupied by isolated spirals of early types. In general, the rotation curves broadly agree with circular rotation, but the pure rotation model fails to account

isolated spirals (24 galaxies) of the M111 sample. It should be noticed that even if the total number of HII regions involved is large (224), they correspond to 15 active galaxies and 10 non-active ones, with unequal weighting for the number of position angles per galaxy. In order to give the same weight to each galaxy, independently of the number of position angles observed, we consider hereafter only the HII regions along the major axes, in such a way that they can be directly compared to the isolated galaxies in M111. Our main result is that disk metallicities of active and control galaxies are the same, since

IC 454

Fig. 35. Velocity distributions for IC 454. The two sets of curves along PA = 140° and PA = 110° correspond to ESO (left) and CAHA (right) data.

NGC 3571

for large scale velocity distribution peculiarities, that can be attributed to the presence of a large scale bar, spiral-arm components, or small-scale central deviations indicative of the presence of non-circular motions and/or decoupled disks. Note that the same kind of small scale central S-shaped deviations from the rotation curve model are found in both active (whether they have a single or double barred host, or are of Sy 1 or Sy 2 type) and non-active galaxies. When enough position angles are available, a better indication can be obtained of whether an inner bar (most cases) or a nuclear disk (see IC 184, NGC 3660, NGC 5728, ESO 139 and NGC 6012) are at the origin of such features.

Fig. 37. Velocity distributions for NGC 3571.

NGC 6012

NGC 7328
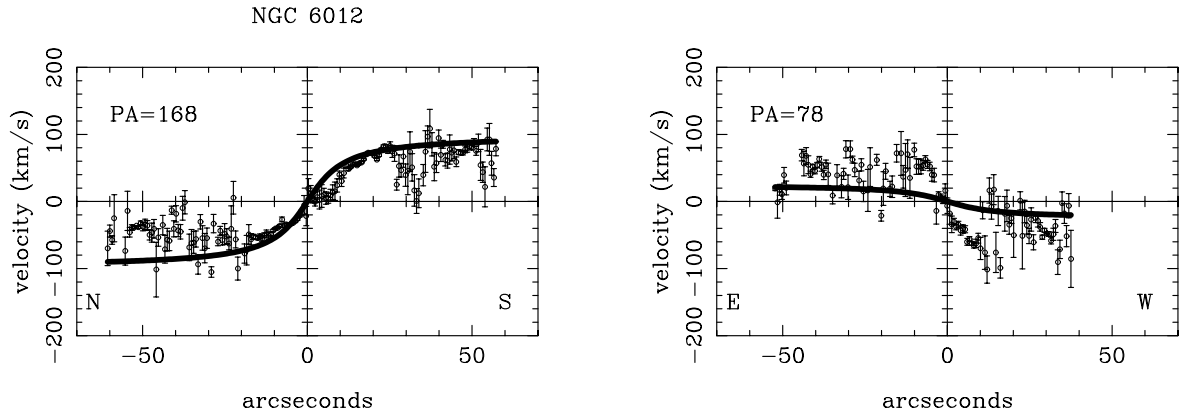
NGC 2712

NGC 3835

Fig. 39. Velocity distributions for NGC 6012.
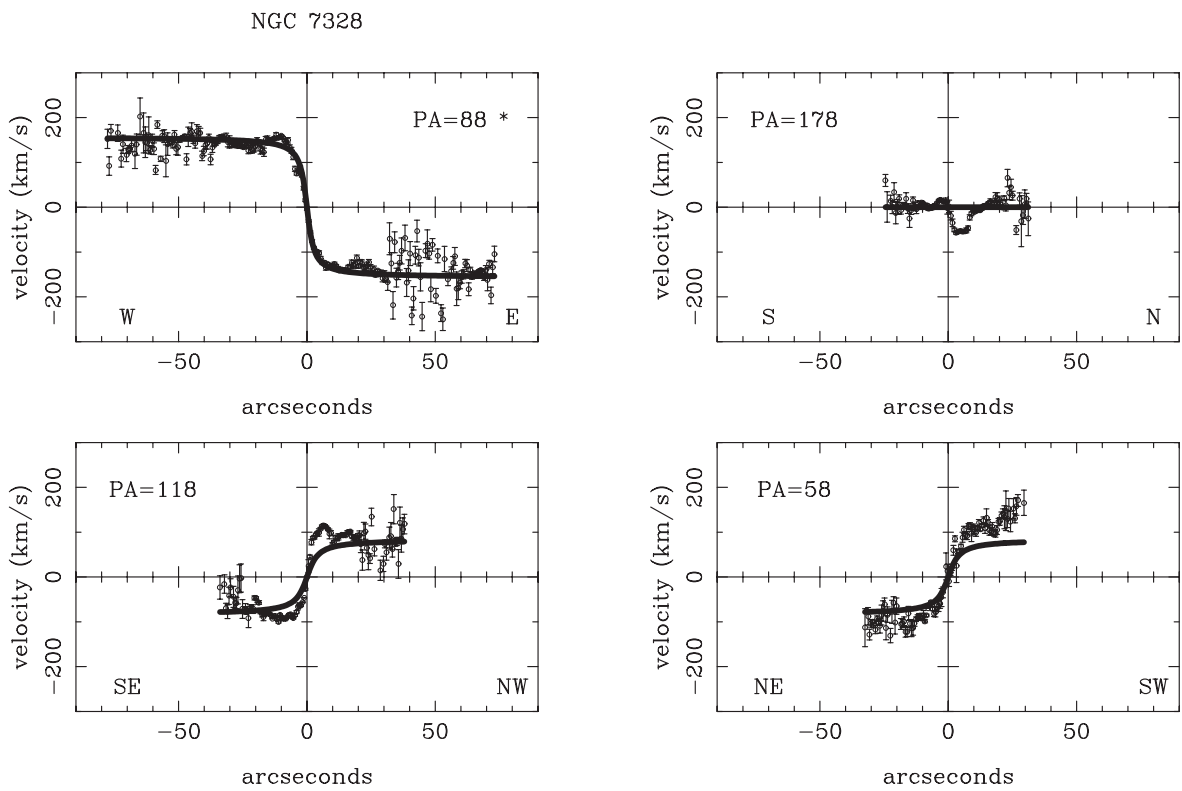
Fig. 41. Velocity distributions for NGC 7328.
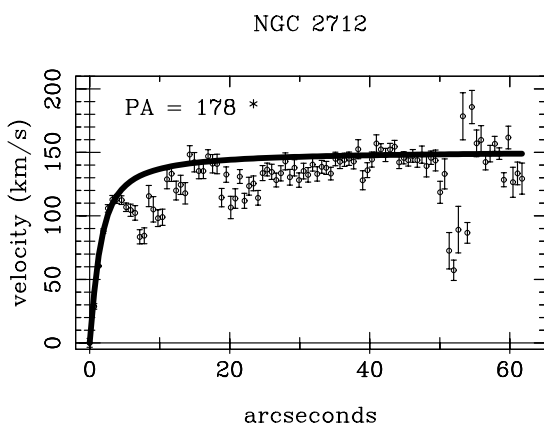
Fig. 43. Average velocity distribution for NGC 2712.
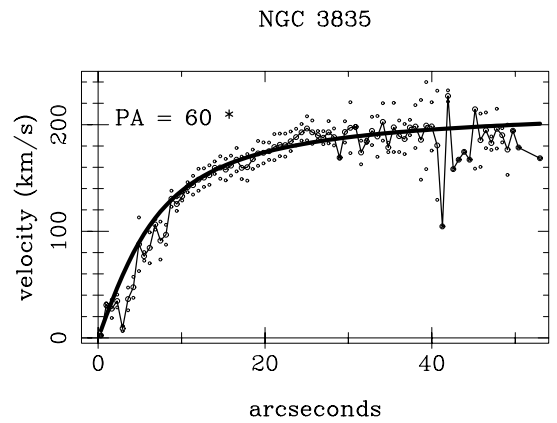
Fig. 45. Average velocity distribution for NGC 3835. The individual points correspond to the data on either side of the nucleus.
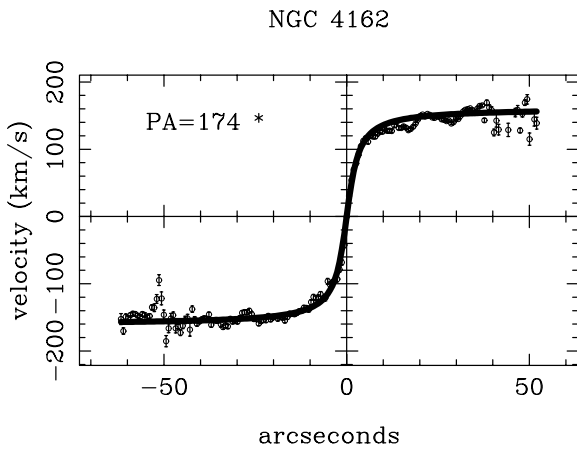
NGC 4162

Fig. 47. Velocity distribution for NGC 4162.
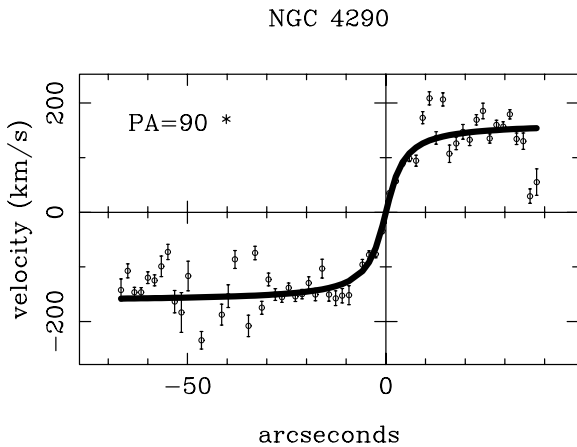
NGC 4290

Fig. 49. Velocity distribution for NGC 4290.
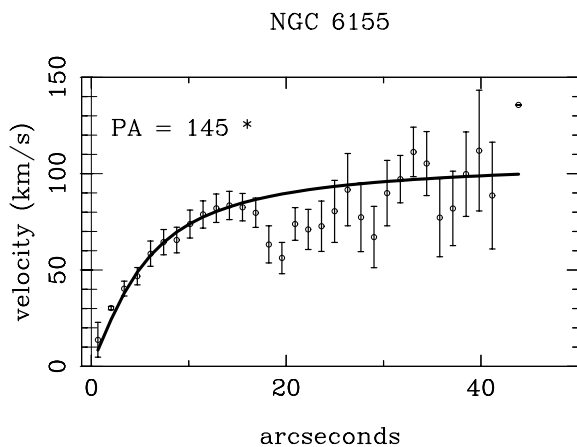
NGC 6155

Fig. 51. Average velocity distribution for NGC 6155.

Disk HII region metallicities, estimated from the [NII]/Hα ratios, are also very similar for the active and non-active sub-samples.

The analysis of the photometric properties of the DEGAS sample obtained from NIR imaging has already shown that active and non-active isolated spiral galaxies share the same disk, bulge and primary bar properties, and that they are indistinguishable at least down to spatial scales of about 300 pc (Márquez et al. 1999, 2000). These results are reinforced here, in the sense that both kinematical properties and disk metallicities lead to the same conclusion. Thus, whether or not they have an AGN, the spiral galaxies in the DEGAS sample are equivalent in all respects (a general discussion based on the DEGAS data will be presented in a forthcoming paper). Therefore, the differences claimed to be related to the mechanisms driving AGN activity should be found in details related to circumnuclear regions still unresolved in our observations. But, interestingly, no significant morphological differences were found, even in the innermost few arcseconds, for a sample of 123 active and non-active galaxies imaged with the HST (Martini et al. 2003). Besides, the AGN activity can involve such different time scales from those of the dynamical processes under study, that any direct connection would be out of scope (see e.g. Hunt & Malkan 1999). Finally, and considering the growing evidence that all galaxies above a certain luminosity host central, massive compact objects (McLure & Dunlop 2002), our results are fully compatible with the idea that the AGN activity could take place recurrently in a given galaxy; in this way, the AGN itself would be seen when fuel is made available in the most internal regions. Note however that our sample is small and that differences between the active and non-active samples may be lost due to the poor statistics; in the recent works by the SLOAN project, for example, several thousand galaxies were required to statistically identify clear differences between active and non active galaxies (Kauffmann et al. 2003).
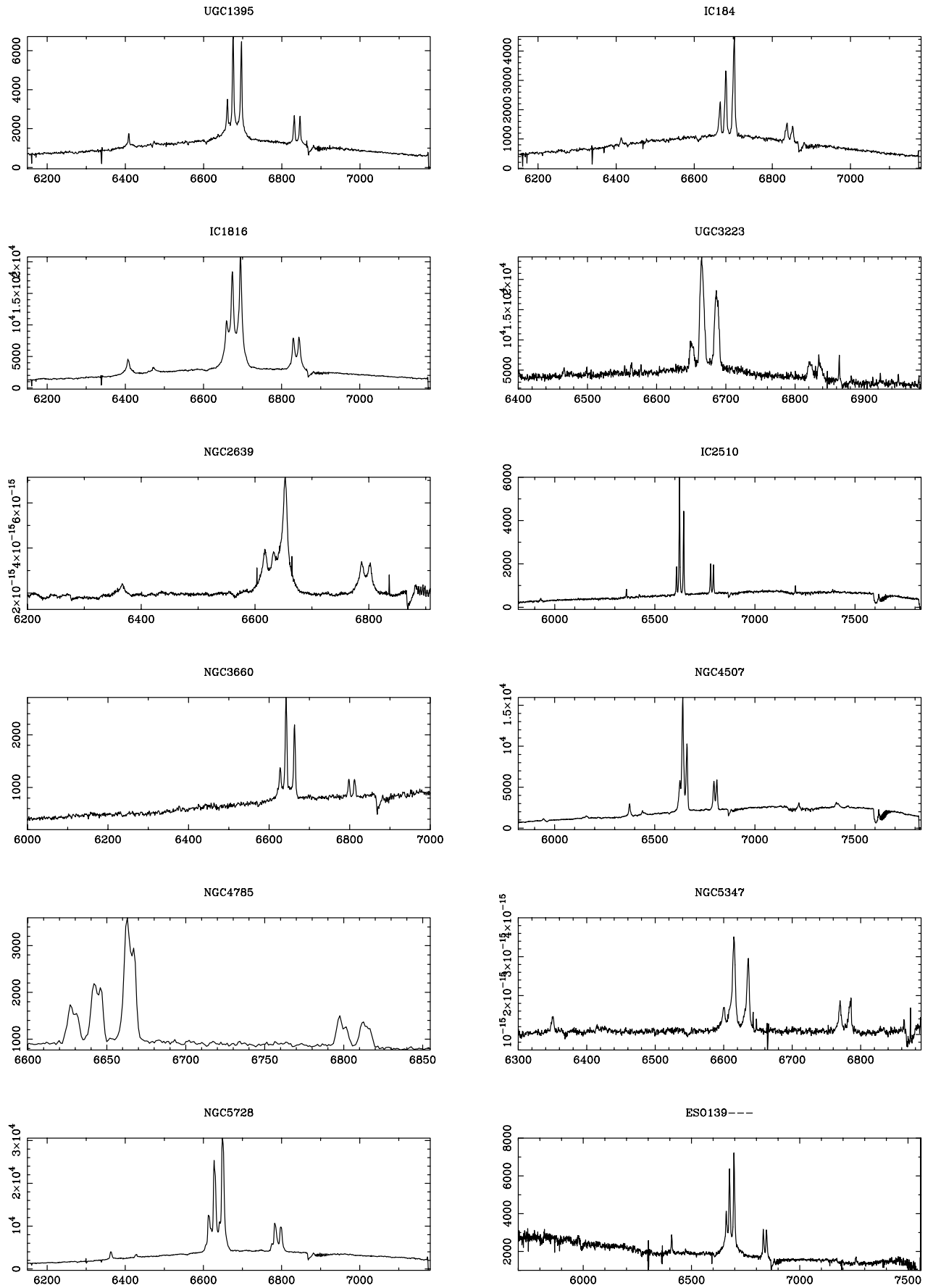
Fig. 53. a. Nuclear spectra, plotted as non calibrated flux vs. observed wavelength (in Å), except for NGC 2639 and NGC 5347 which are flux calibrated (in erg s^{-1} cm^{-2} Å^{-1}).
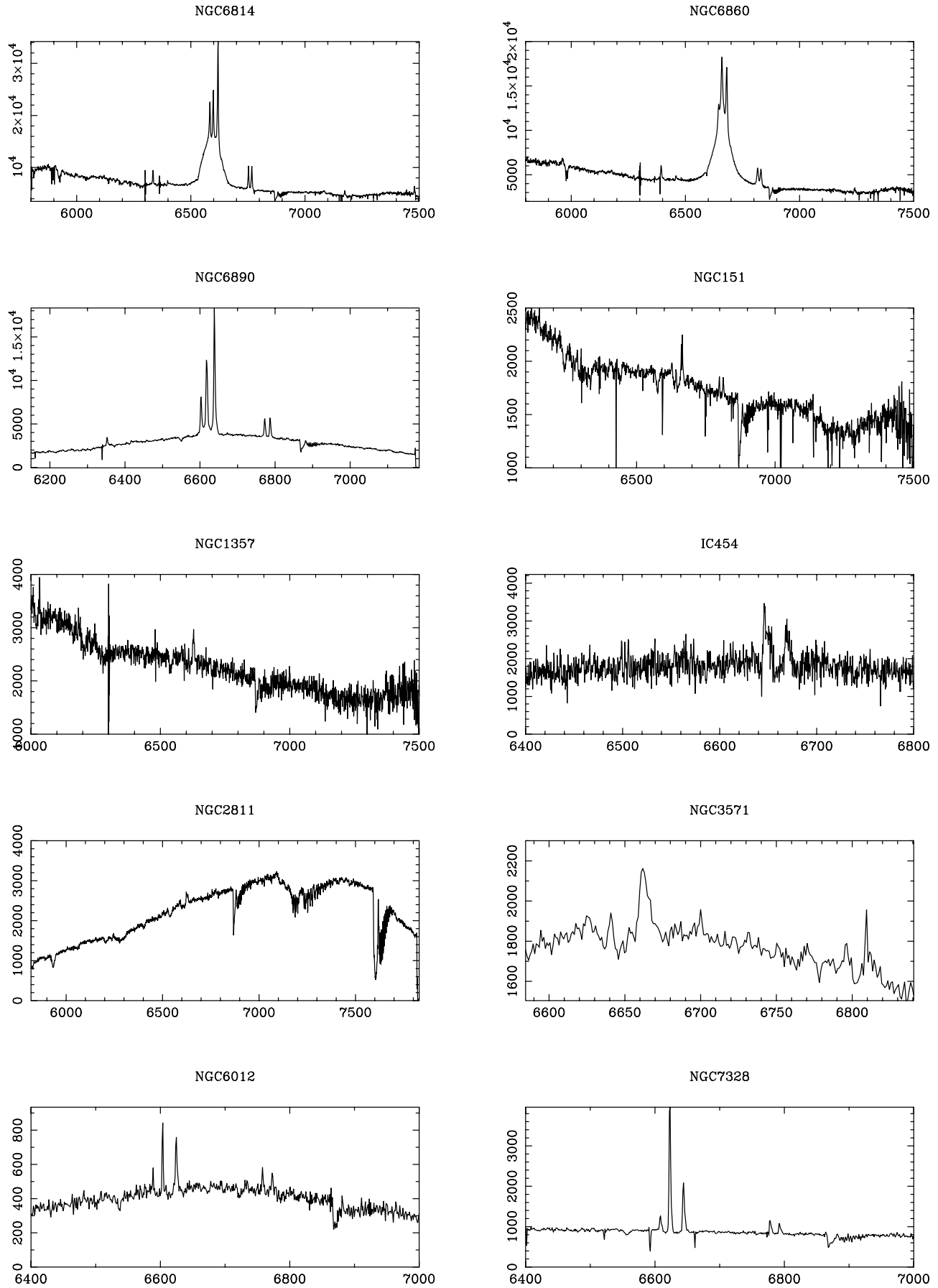
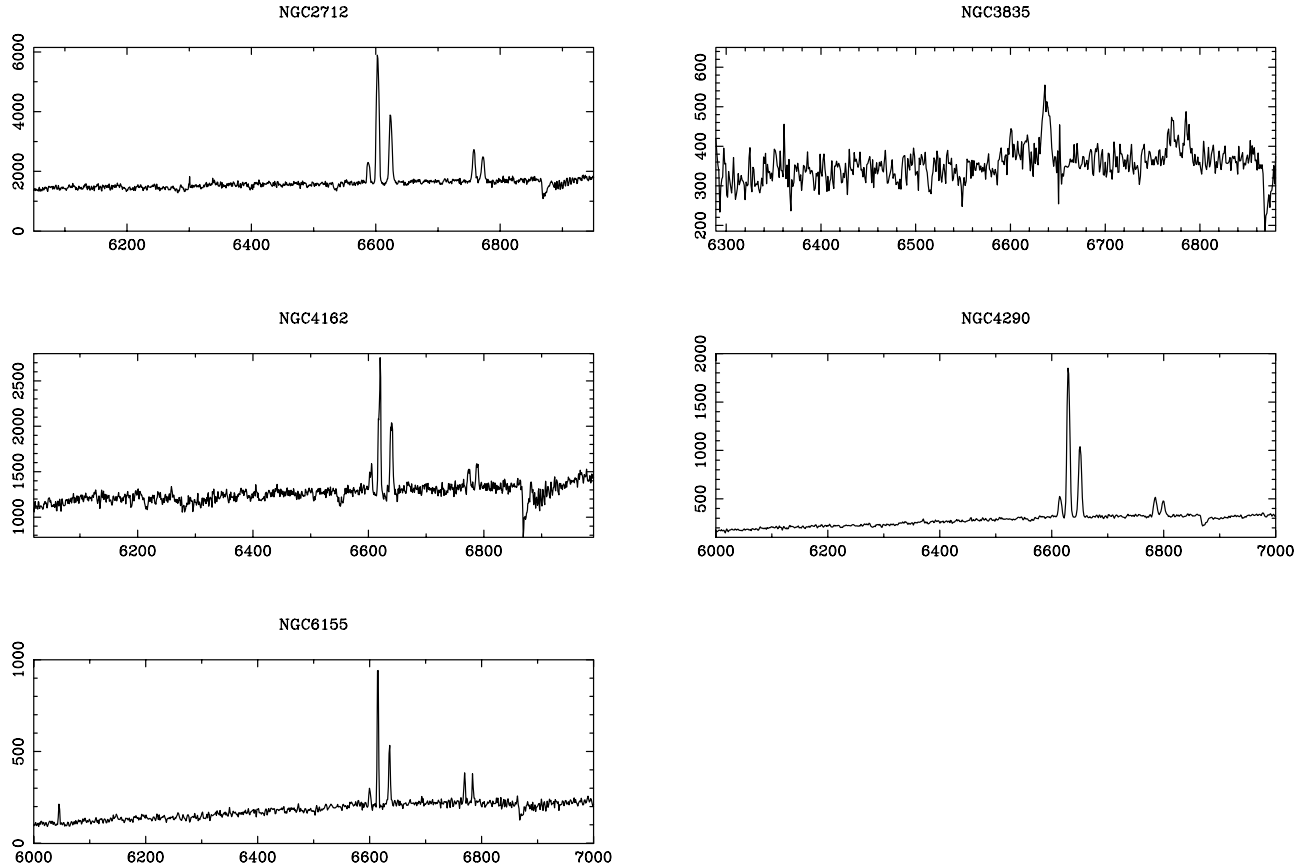**Fig. 53.** b. Nuclear spectra, plotted as non calibrated flux vs. observed wavelength (in Å).

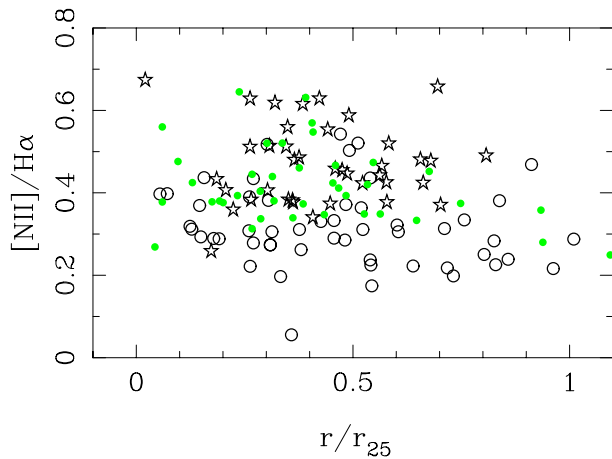**Fig. 53.** c. Nuclear spectra, plotted as non calibrated flux vs. observed wavelength (in Å).

Fig. 54. [NII]/Hα intensity ratio as a function of distance of HII region to the nucleus, normalized to r_{25} for the DEGAS sample (with stars for active galaxies and filled circles for non-active objects) and for the isolated spirals in M111 (empty circles) having the same absolute magnitude distribution ($-22 < M_B < -19$) (see text).

References

Courteau, S. 1997, AJ, 114, 2402

Emsellem, E., Greusard, D., Combes, F., et al. 2001, A&A, 368, 52

Héraudeau, P., & Simien, F. 1998, A&AS, 133, 317

Ho, L. C., Filippenko, A. V., & Sargent, W. L. W. 1997, ApJS, 112, 315

Hunt, L. K., & Malkan, M. A. 1999, ApJ, 516, 660

Kauffmann, G., Heckman, T. M., Tremonti, C., et al. 2003, MNRAS, 346, 1055

Kollatschny, W., & Fricke, K. J. 1987, A&A, 183, 9

Márquez, I., & Moles, M. 1996, A&AS, 120, 1

Márquez, I., Durret, F., González Delgado, R. M., et al. 1999, A&AS, 140, 1

Márquez, I., Durret, F., Masegosa, J., et al. 2000, A&A, 360, 431

Márquez, I., Masegosa, J., Moles, M., et al. 2002, A&A, 393, 389

Márquez, I., Masegosa, J., Durret, F., et al. 2003, A&A, 409, 459

Martini, P., Regan, M. W., Mulchaey, J. S., & Pogge, R. W. 2003, ApJ, 589, 774

McLure, R. J., & Dunlop, J. S. 2002, MNRAS, 331, 795

Melnick, J., Terlevich, R., & Moles, M. 1986, in Luminous Stars and Associations in Galaxies, ed. C. W. H. De Loore, A. Wilkis, & P. Laskarides (Dordrecht: Reidel), 505

Moles, M., Márquez, I., & Pérez, E. 1995, ApJ, 438, 604

Pérez, E., Márquez, I., Marrero, I., et al. 2000, A&A, 353, 893

Persic, M., & Salucci, P. 1995, ApJS, 99, 501

Pogge, R. W., & Martini, P. 2002, ApJ, 569, 624

Prada, F., & Gutiérrez, C. M. 1999, ApJ, 517, 123

Schommer, R. A., Caldwell, N., Wilson, A. S., et al. 1988, ApJ, 324, 154

de Vaucouleurs, G., de Vaucouleurs, A., Corwin, H. G. Jr, et al. 1991, Third Reference Catalogue of Bright Galaxies, XII (1-3), 2069 (Springer-Verlag) (RC3)

Véron-Cetty, M. P., & Véron, P. 2001, A&A, 375, 791

Online Material

Table 3. Detailed log of the spectra.

Galaxy (Active)	Run	PA (°)	Exp. Time (s)	Galaxy (Non-active)	Run	PA (°)	Exp. Time (s)
UGC 1395	WHT 96	35	1800, 1800	NGC 151	LC 898	75	2400
		125	0, 3600			151	2400
	WHT 99	80	3600, 1800			165	2400
	LC 896	135	3600	NGC 1357	LC 898	85	1860
	LC 898	45	2400	IC 454	CAHA 00	110	3600, 1800
	LC 898	165	2400			140	3600, 1800
IC 184	WHT 99	7	3600, 3600		ESO 96	50	3600
		97	3600, 1800			110	3600
	LC 896	7	3600			140	3600
		37	2400			170	3000
		97	3600	NGC 2811	ESO 96	20	3000
		157	2400			50	2400
IC 1816	LC 896	0	2400			110	3600
		90	2400			170	2400
UGC 3223	WHT 99	80	3600, 1800	NGC 3571	LC 596	94	3600
	ESO 96	50	3600			64	3600
		80	3600			4	3600
		110	2400	NGC 6012	LC 896	78	2400
		170	3600			168	2400
	CAHA 00	20	3600, 3600	NGC 7328	LC 896	88	2400
		170	3600, 1800			178	2400
NGC 2639	WHT 99	0	1800, 1800		LC 898	58	3600
		45	3600, 1800			118	2400
		315	3600, 1800				
IC 2510	ESO 96	58	3600				
		118	3600				
		148	3600				
		178	3000				
NGC 3660	WHT 99	115	3600, 1800				
	ESO 96	25	3600				
		85	2400				
		115	3600				
		145	2400				
	CAHA 00	25	3600, 1800				
	WHT 00	85	3600, 1800				
NGC 4507	ESO 96	51	3600				
		141	3340				
NGC 4785	LC 596	9	1650				
		81	3600				
NGC 5347	WHT 00	310	3600, 1800				
NGC 5728	LC 896	0	2400				
		35	2400				
		90	3600				
		150	3600				
ESO 139-12	LC 596	35	3600				
		65	3600				
		125	3600				
	LC 896	0	3600				
		30	3600				
		60	2400				
		120	3600				
	LC 898	5	2400				
NGC 6814	WHT 96	30	1800, 1800				
		120	1800, 3600				
	WHT 00	60	1800, 1800				
	LC 896	29	3600				
		119	2400				
	LC 898	20	2400				
NGC 6860	LC 896	4	3600				
		34	3600				
		64	3600				
		124	2400				
	LC 898	16	2400				
NGC 6890	LC 896	2	2400				
		62	3600				
		122	2400				
		152	3600				
	LC 898	13	2400				

For the WHT and CAHA runs the two exposure times correspond to Hβ and Hα respectively, the exposure time for the CaT being the sum of the two. The CaT WHT00 data for NGC 6814 and all the CaT CAHA00 data did not have sufficient signal to noise ratio to allow us to derive the stellar velocity distributions.

UGC 1395
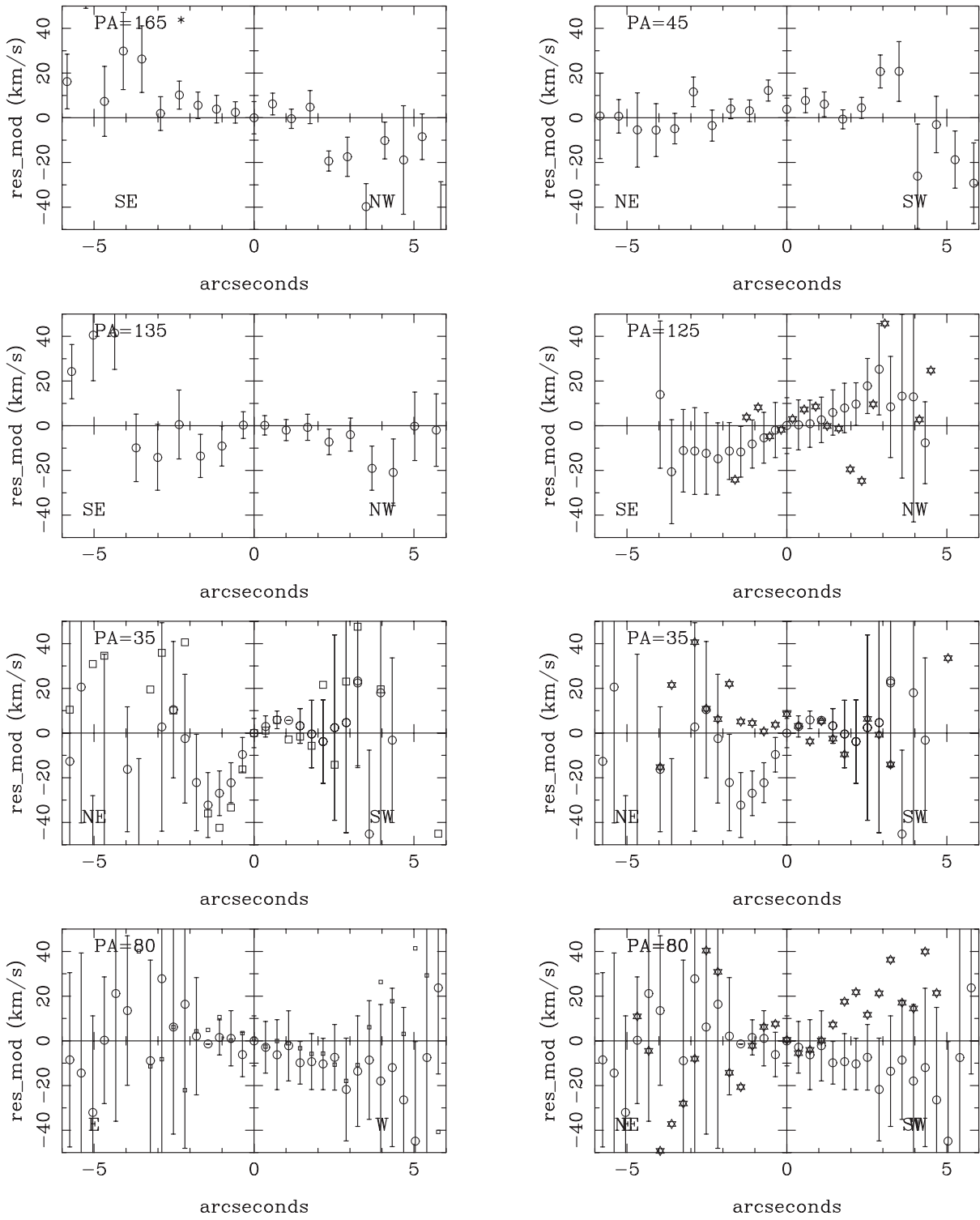
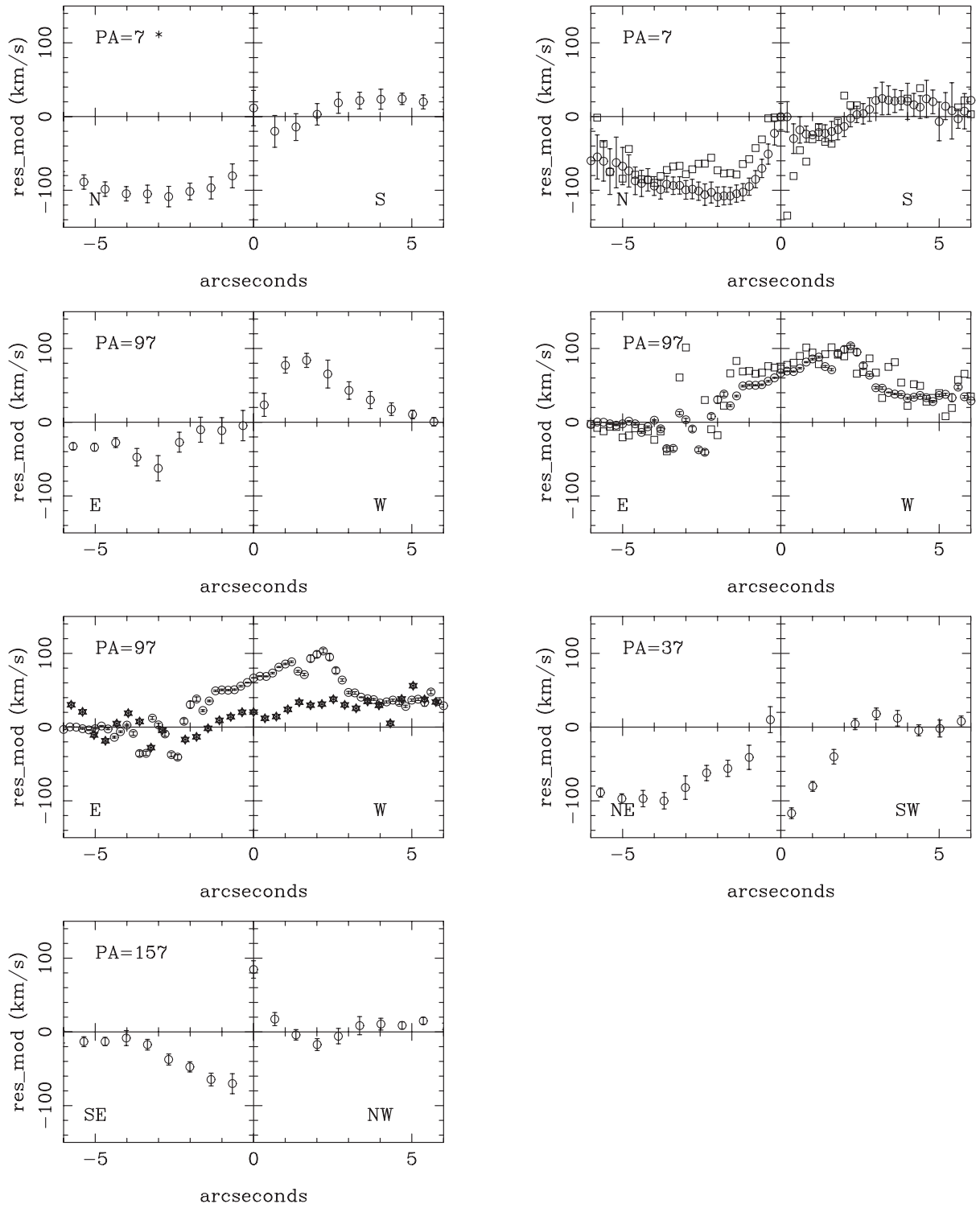**Fig. 3.** Residuals from the model for UGC 1395.

IC 184

Fig. 5. Residuals from the model for IC 184.
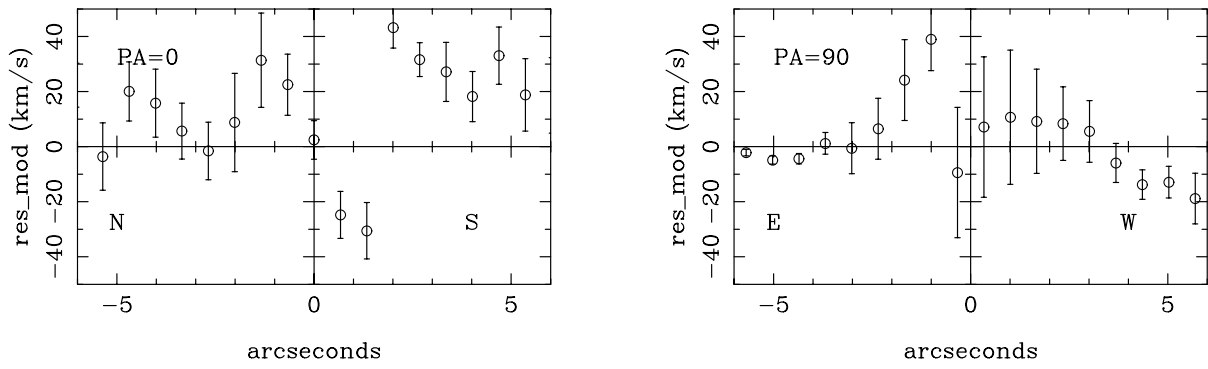
IC 1816

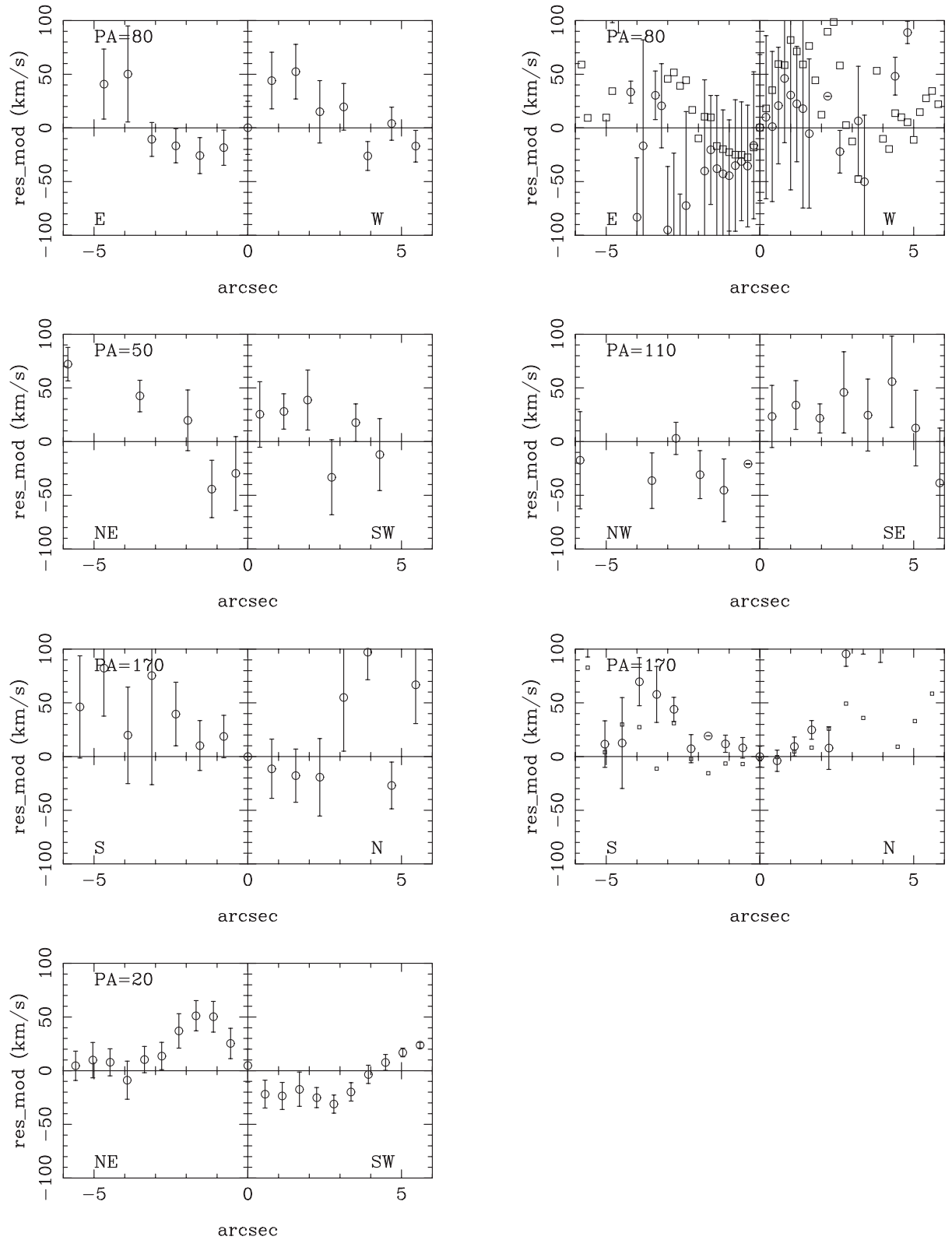**Fig. 7.** Residuals from the model for IC 1816.

UGC 3223

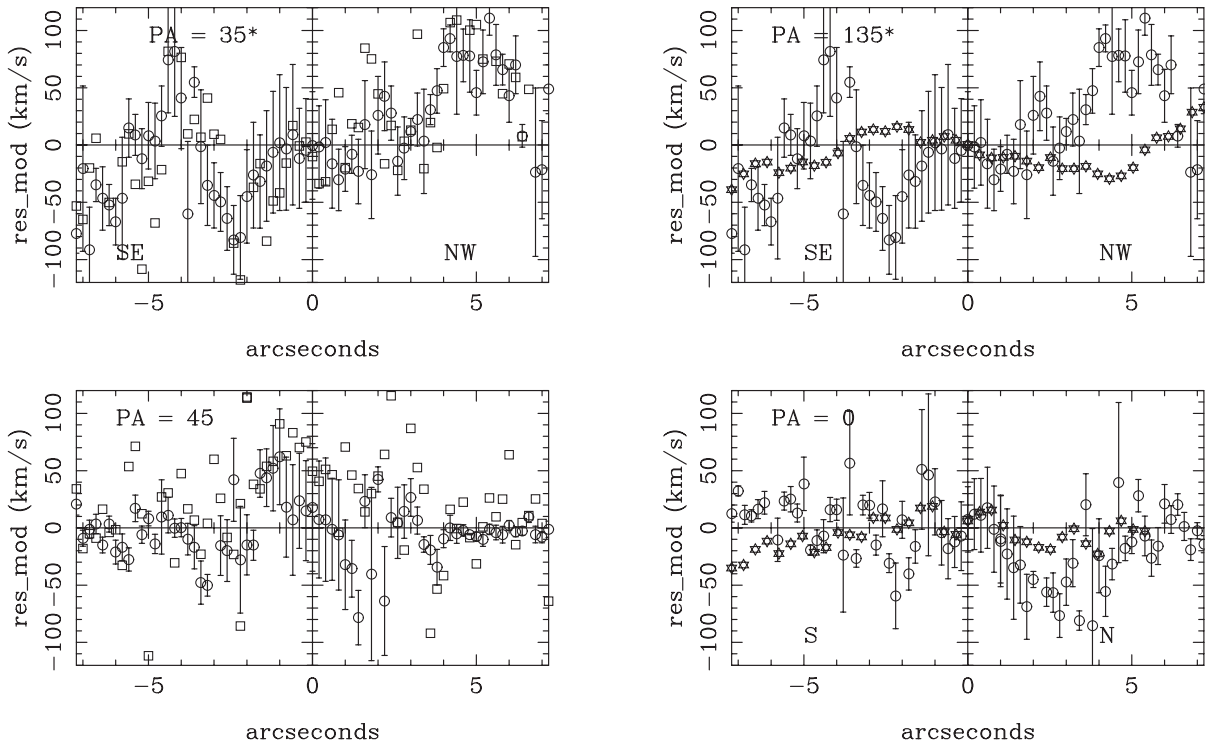**Fig. 9.** Residuals from the model for UGC 3223.

NGC 2639

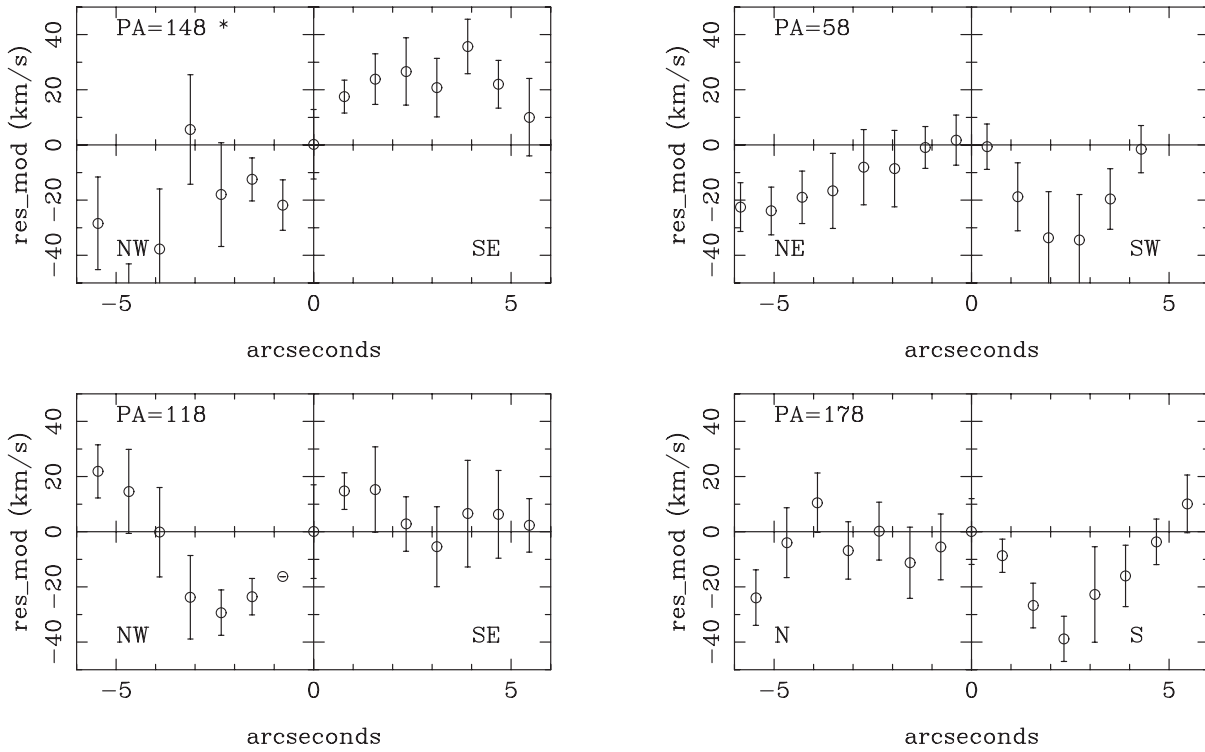**Fig. 11.** Residuals from the model for NGC 2639.

IC 2510

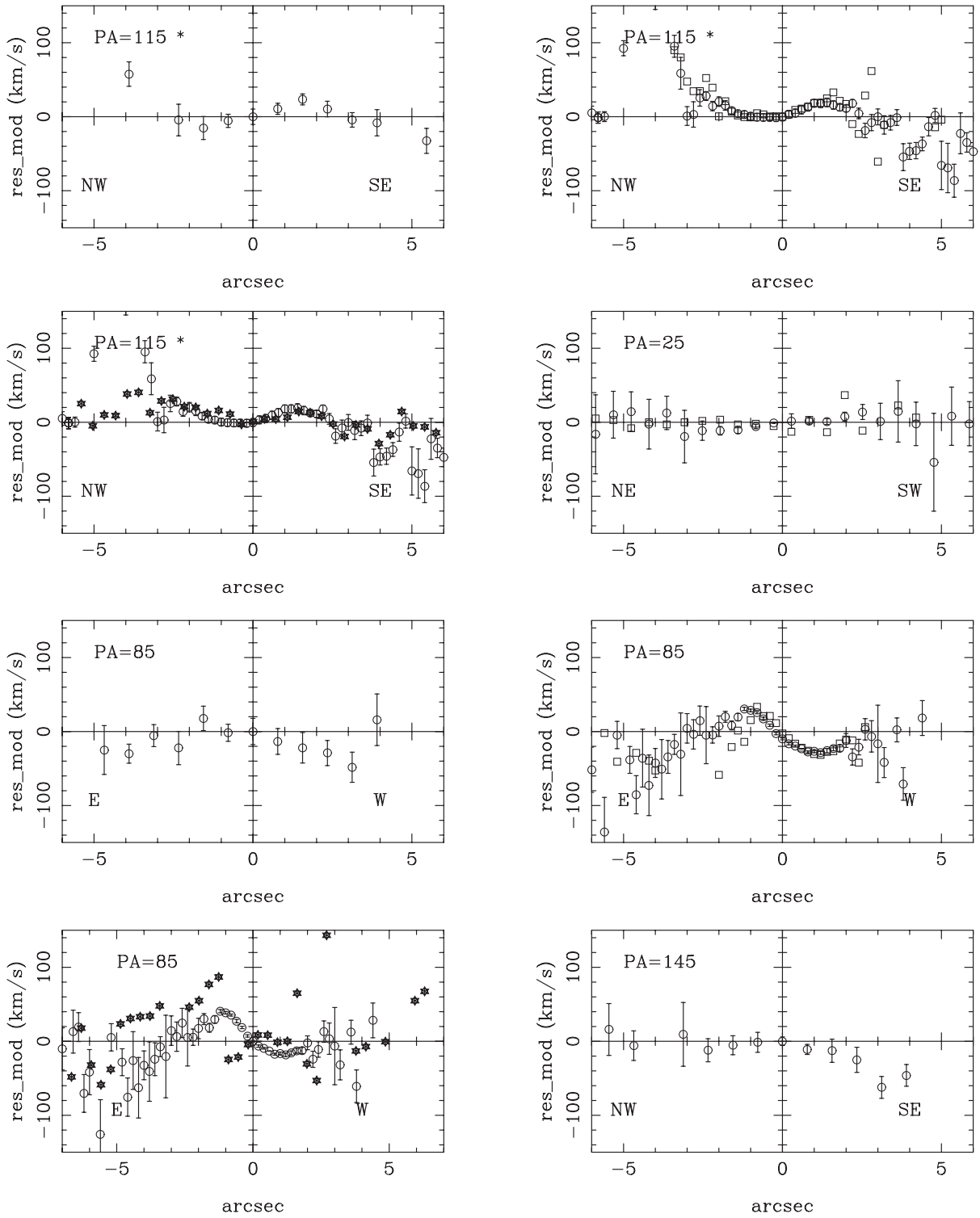**Fig. 13.** Residuals from the model for IC 2510.

NGC 3660

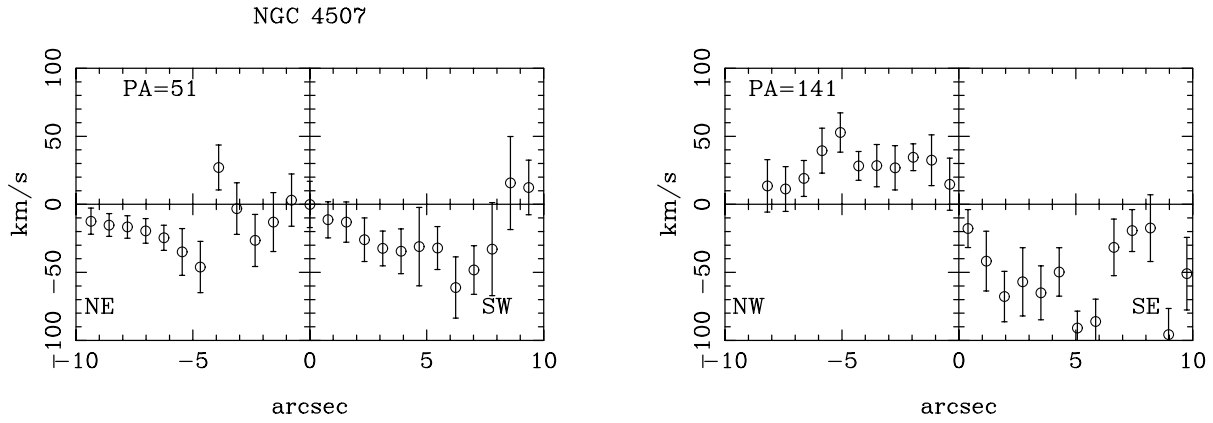**Fig. 15.** Residuals from the model for NGC 3660.

NGC 4507

Fig. 17. Residuals from the model for NGC 4507.
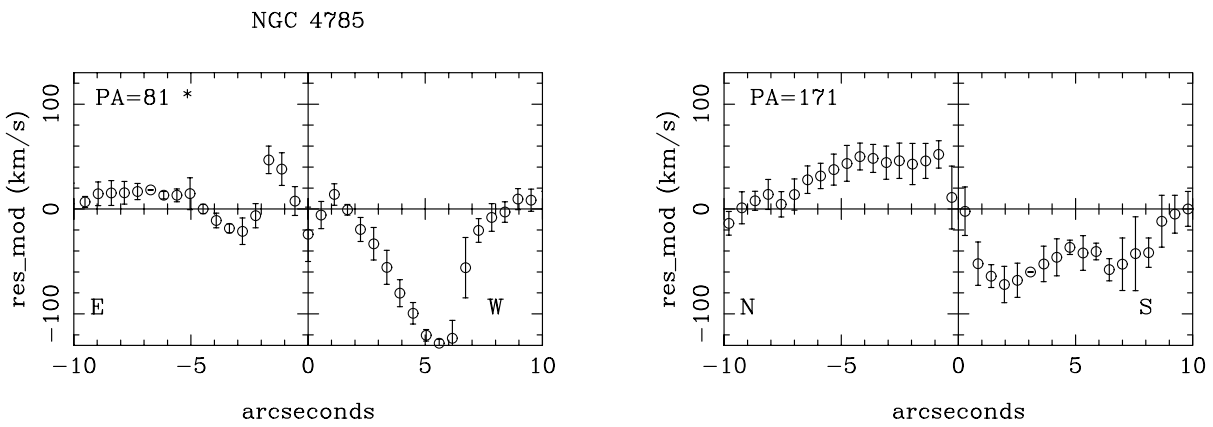
NGC 4785

Fig. 19. Residuals from the model for NGC 4785.
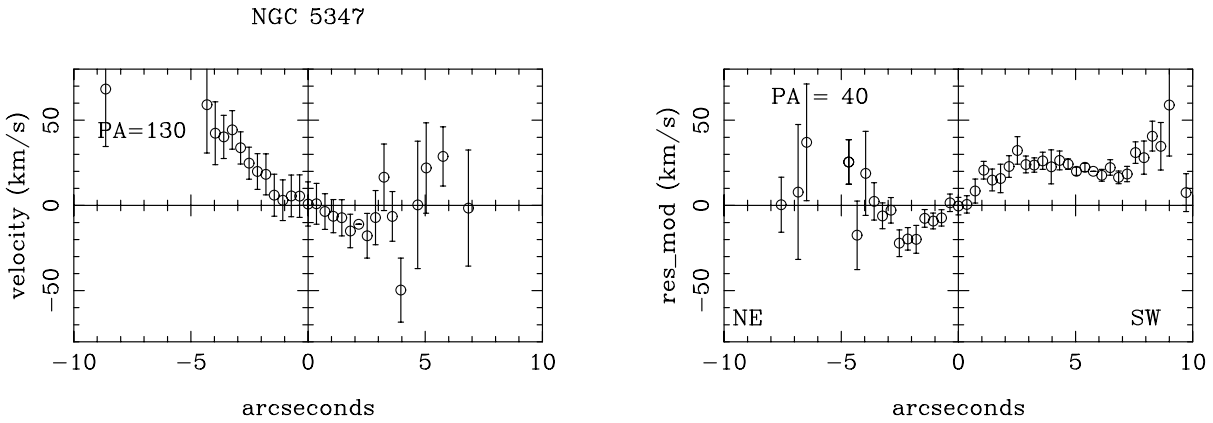
NGC 5347

Fig. 21. Residuals from the model for NGC 5347.

NGC 5728
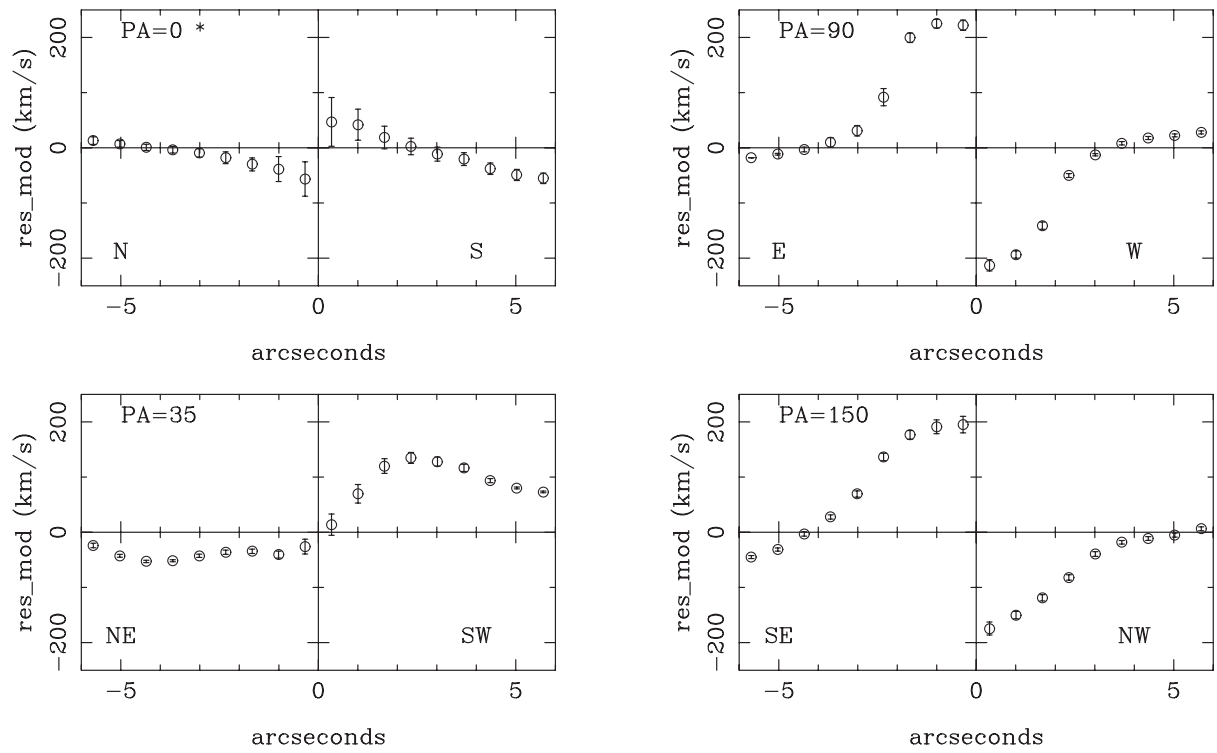
Fig. 23. Residuals from the model for NGC 5728.

ESO 139
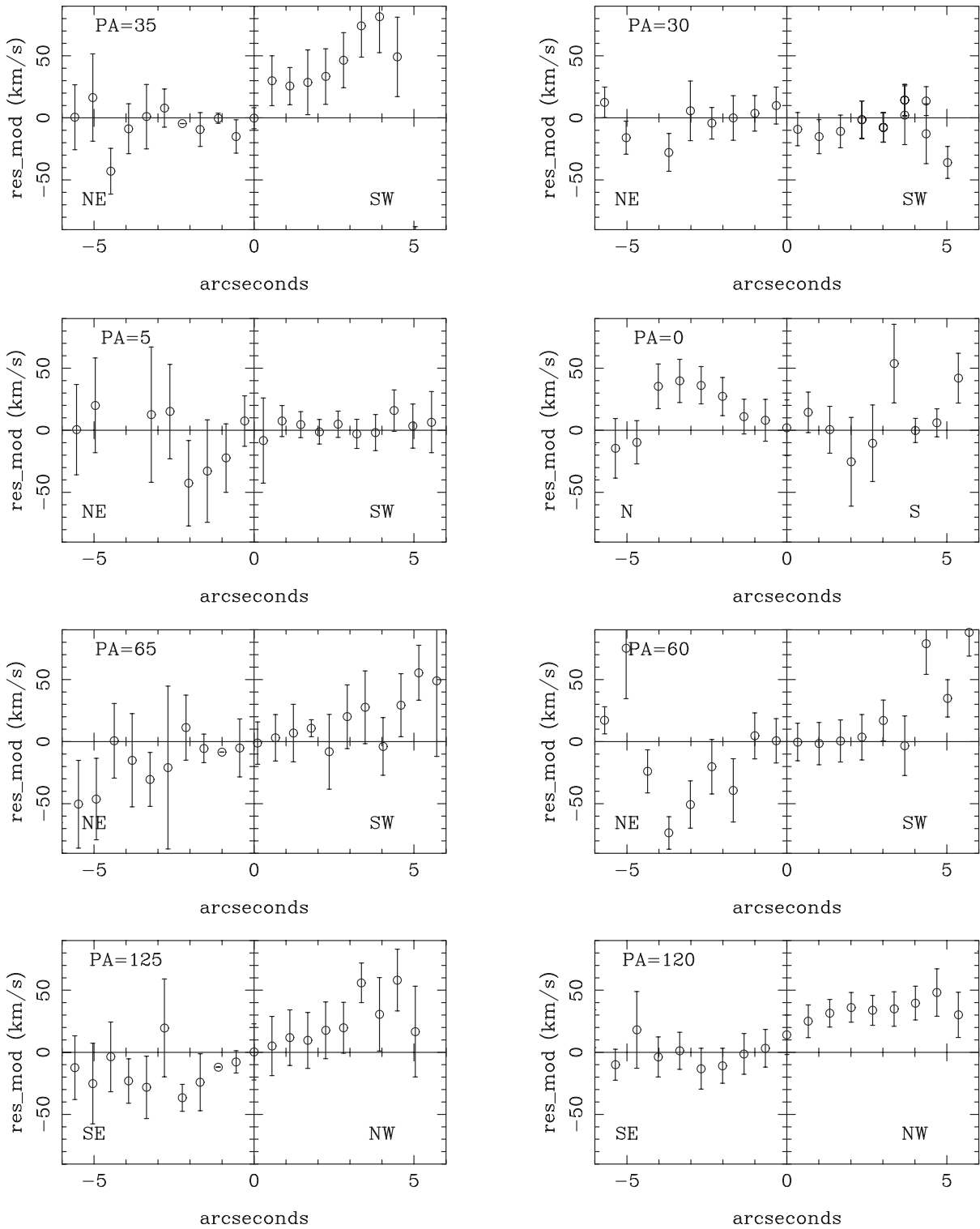
Fig. 25. Residuals from the model for ESO 139-G12.

NGC 6860
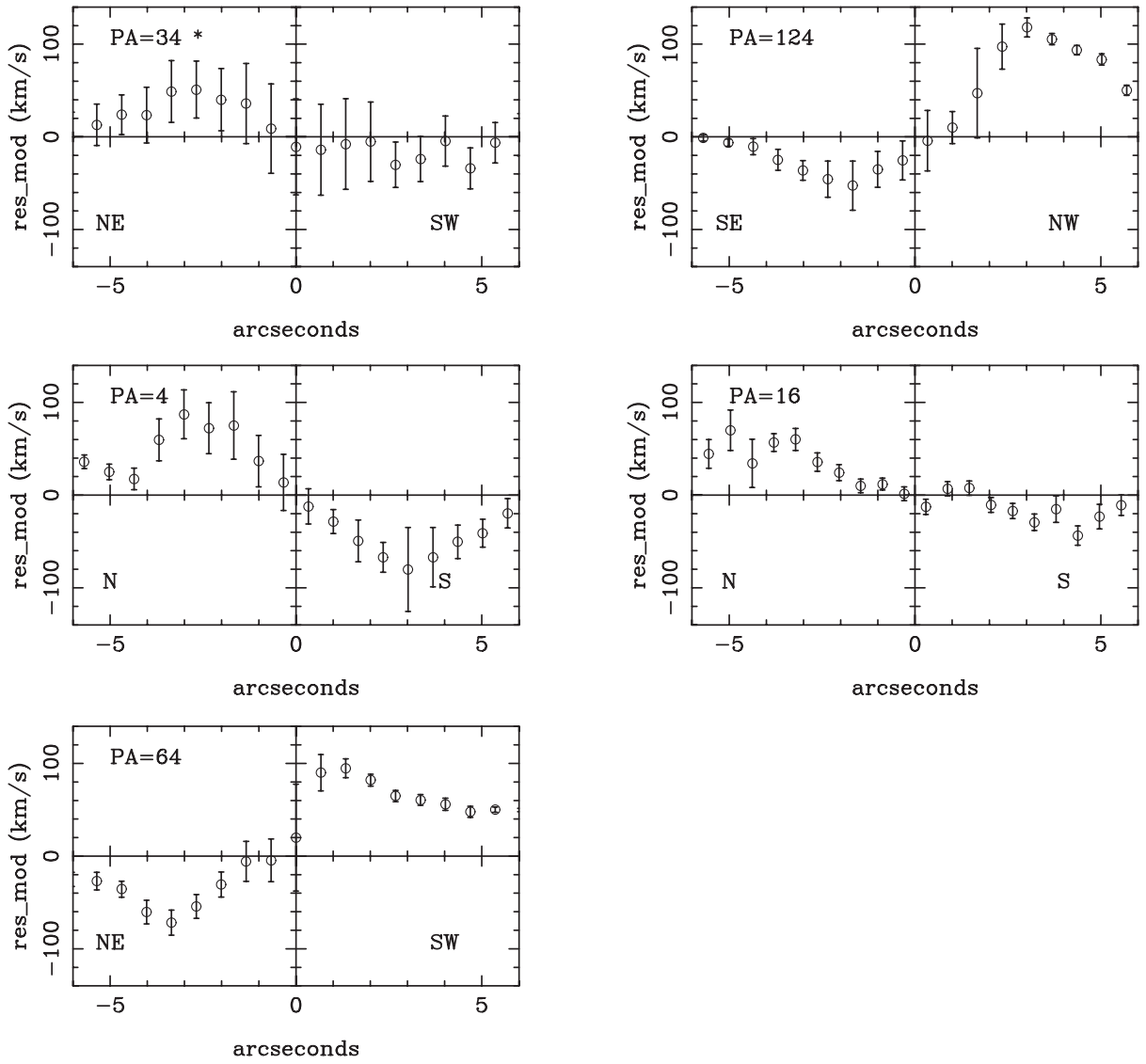
Fig. 28. Residuals from the model for NGC 6860.

NGC 6890
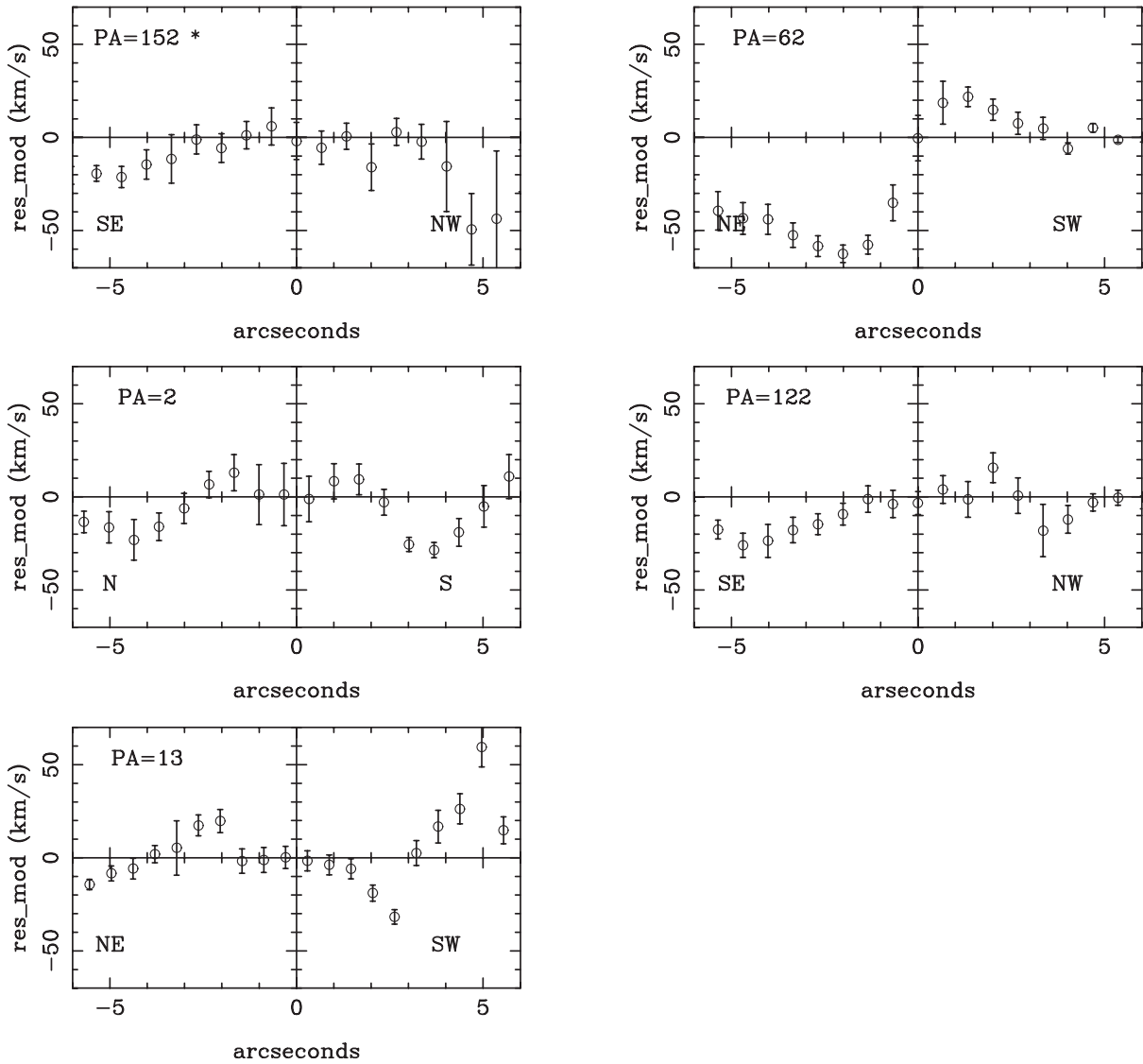
Fig. 30. Residuals from the model for NGC 6890.

NGC 151
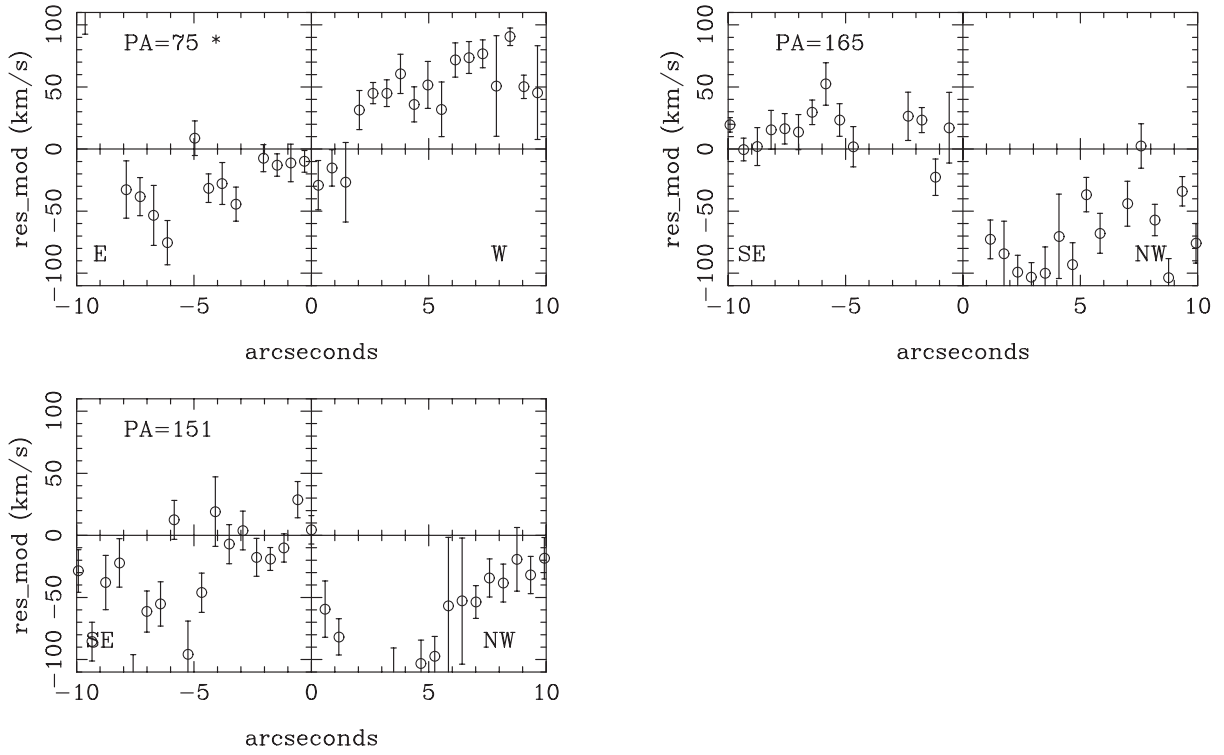
Fig. 32. Residuals from the model for NGC 151.

NGC 1357
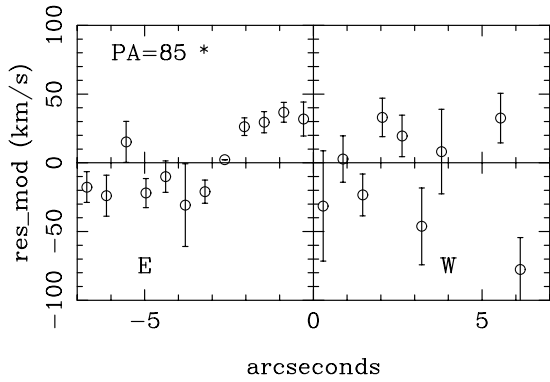
Fig. 34. Residuals from the model for NGC 1357.

IC 454
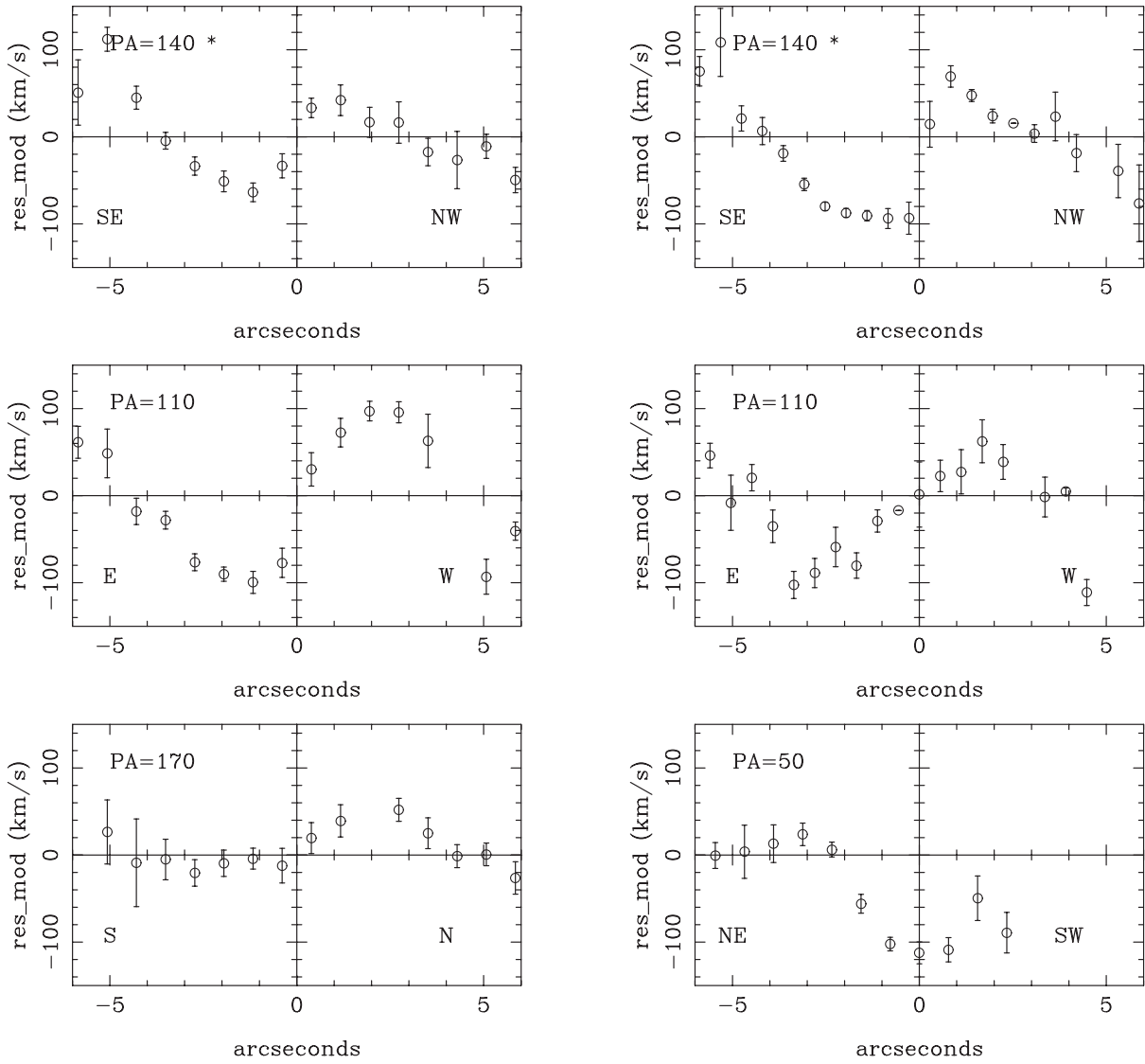
Fig. 36. Residuals from the model for IC 454.

NGC 3571
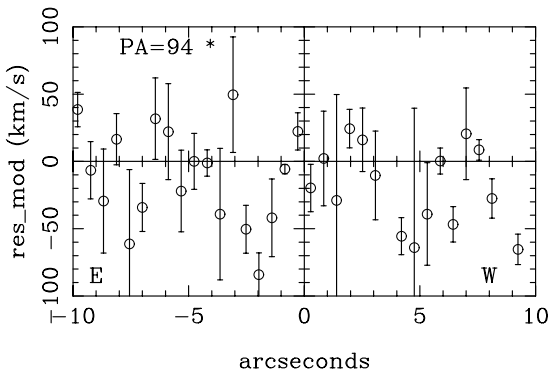
Fig. 38. Residuals from the model for NGC 3571.
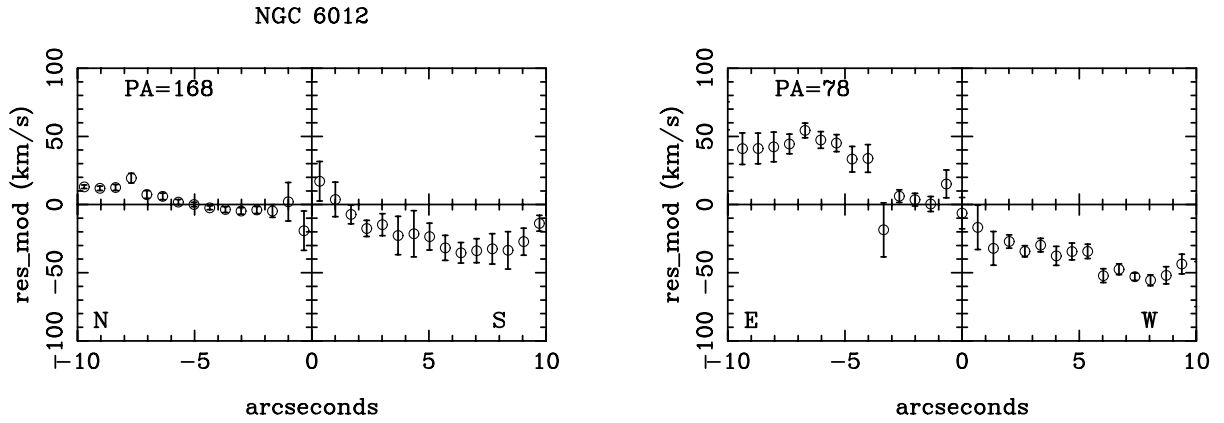
NGC 6012

Fig. 40. Residuals from the model for NGC 6012.
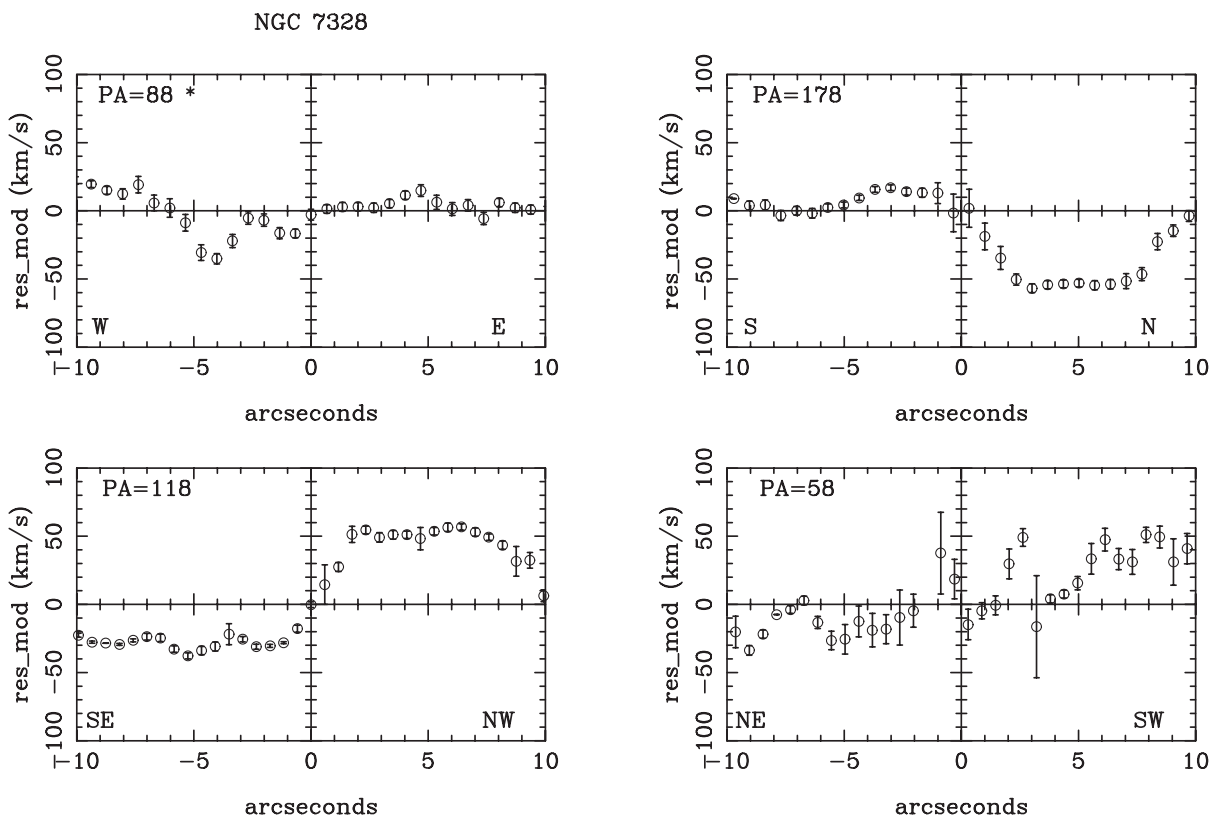
NGC 7328

Fig. 42. Residuals from the model for NGC 7328.
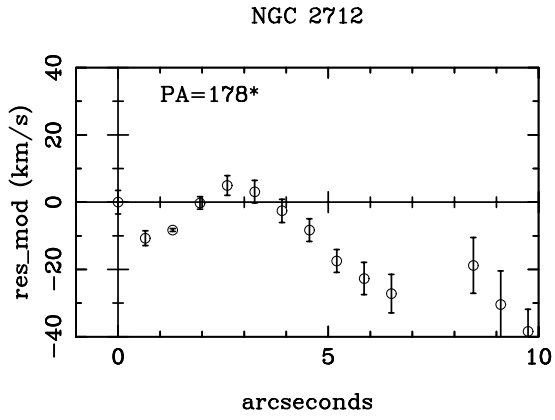
NGC 2712

Fig. 44. Residuals from the model for NGC 2712.

NGC 3835

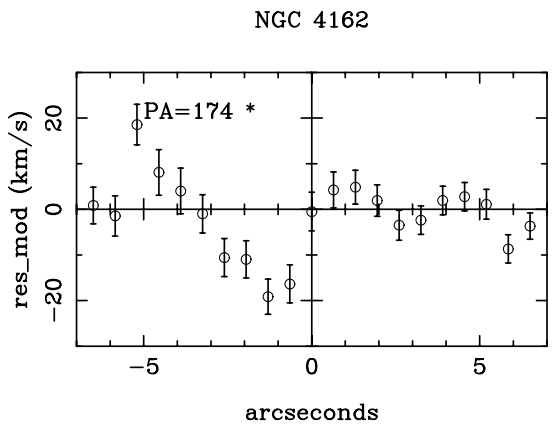**Fig. 46.** Residuals from the model for NGC 3835.

NGC 4162

Fig. 48. Residuals from the model for NGC 4162.
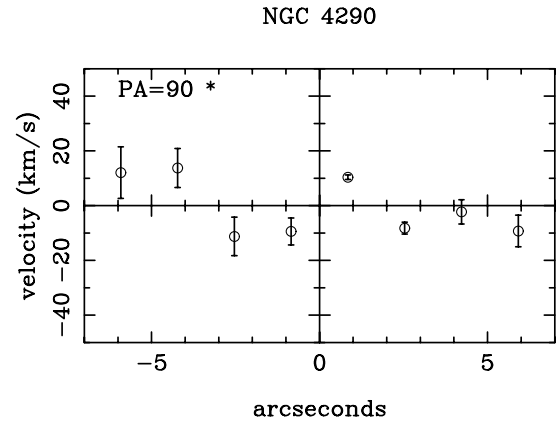
NGC 4290

Fig. 50. Residuals from the model for NGC 4290.
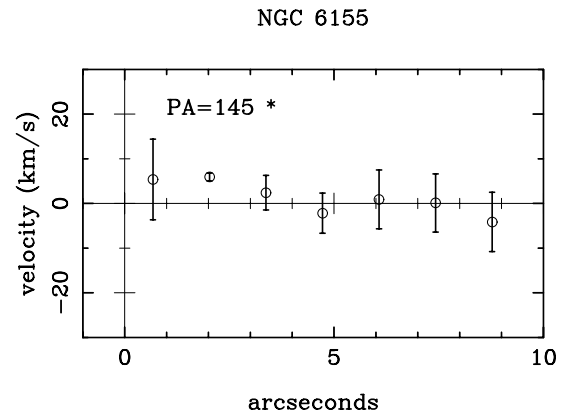
NGC 6155

Fig. 52. Residuals from the model for NGC 6155.